

## AD-A274 167

TION PAGE

Form Approved  
OAS No. 0704-0168

average 1 hour per release, including the time for reviewing instructions, searching existing data sources, gathering the collection of information. Send comments regarding this burden estimate or any other aspect of this collection of information, including suggestions for reducing this burden estimate, to Washington Headquarters Services, Directorate for Information Operations and Reports, 1215 Jefferson Avenue, Management and Budget, Paperwork Reduction Project (0704-0168), Washington, DC 20503.

1. AGENCY USE ONLY (Leave blank)		2. REPORT DATE 27 Sep 93		3. REPORT TYPE AND DATES COVERED Final Tech 01May90 to 30Apr93	
4. TITLE AND SUBTITLE Interface Phenomena in Metal-Ceramic Composites				5. FUNDING NUMBERS G1102F 2306/AS 0279 (G) AFOSR-90-0279	
6. AUTHOR(S) Rishi Raj				7. PERFORMING ORGANIZATION REPORT NUMBER AFFINAL93	
7. PERFORMING ORGANIZATION NAME(S) AND ADDRESS(ES) Cornell University Department of Materials Science and Engineering AFOSR-R Ithaca NY 15853-1501				8. SPONSORING/MONITORING AGENCY NAME(S) AND ADDRESS(ES) AFOSR/NE Building 410 Bolling AFB DC 20332-6448 Attn: Dr. Charles Ward	
9. SPONSORING/MONITORING AGENCY NAME(S) AND ADDRESS(ES) AFOSR/NE Building 410 Bolling AFB DC 20332-6448 Attn: Dr. Charles Ward				10. SPONSORING/MONITORING AGENCY REPORT NUMBER AFOSR-90-0279	
11. SUPPLEMENTARY NOTES					
12a. DISTRIBUTION/AVAILABILITY STATEMENT Approved for public release; distribution unlimited.					
13. ABSTRACT (Maximum 200 words) This report describes theoretical and experimental results that link the properties of the heterointerface to the macroscopic mechanical behavior of metallic composites where the continuous phase is a metal and the hard phase is a ceramic (MMCs) or an intermetallic (IMCs). The results emphasize that the properties of the composites depend on the interaction between cohesive strength of the M/C or M/I interface and the physical microstructural scale of the metal. This result is general and is expected to apply from room temperature properties, such as toughness, to creep resistance at very high temperatures. At room temperature the effect of scale is based on the dislocation pile-up model for delamination at the interface. At high temperatures the climb rate of dislocations in the metal layer depends on its width and on the pinning efficiency of lattice dislocations at the interface.					
14. SUBJECT TERMS Interfaces, MMC, Intermetallics, Oxidation, Grain Boundary Sliding, Composites, Fracture				15. NUMBER OF PAGES 49	
17. SECURITY CLASSIFICATION OF REPORT				18. SECURITY CLASSIFICATION OF THIS PAGE	
19. SECURITY CLASSIFICATION OF ABSTRACT				20. LIMITATION OF ABSTRACT	

**Best  
Available  
Copy**

## Table of Contents

### Abstract

<b>1. In-Situ Stress Strain Response of Small Metal Particles Embedded in a Ceramic Matrix</b>	<b>2</b>
1.1 ABSTRACT (2)	
1.2 INTRODUCTION (2)	
1.2 EXPERIMENTAL TECHNIQUE (4)	
1.3. ANALYSIS OF THE TRACTION ON THE SURFACE OF THE BRIDGED CRACK (6)	
1.4. RESULTS (9)	
1.5 DEBONDING AT THE METAL-CERAMIC INTERFACE (15)	
1.6 SUMMARY (18)	
<b>2. The Influence of Microstructural Scale On Toughening of Metallic Composites</b>	<b>19</b>
2.1 ABSTRACT (19)	
2.1 METALLIC COMPOSITES OF DIFFERENT MICROSTRUCTURAL SCALE (19)	
2.1.1 Large Scale Metal/Ceramic Composites (19)	
2.1.1 Types of Small Scale Metal/Ceramic Composites (20)	
2.2 TRENDS IN TOUGHENING ON THE MICROMETER SCALE (27)	
2.3 "MICRO" VS. "MACRO" COMPOSITE BEHAVIOR (31)	
<b>3. Single Crystal Based Microstructure Design of Metal Matrix Composites for High Temperature Applications</b>	<b>32</b>
3.1 ABSTRACT (32)	
3.2 INTRODUCTION (33)	
3.2.1 The Design of Superalloys (34)	
3.2.2 The Design of Ceramic Reinforced Metal Matrix Composites (35)	
3.3 SINGLE CRYSTAL DESIGN FOR CREEP RESISTANCE (36)	
3.3.1 Diffusional Creep (38)	
3.3.2 Dislocation Creep (41)	
3.3 RESISTANCE TO THERMAL SHOCK (44)	
3.4 THE ROLE OF THE ATOMIC BONDING AND STRUCTURE OF M/C INTERFACE (46)	
3.5 SUMMARY (46)	
<b>4. List of Publications and Patent</b>	<b>48</b>
<b>5. Graduate Students</b>	<b>49</b>

93-31199



93 12 27 05.2

## 1. Abstract

This report describes theoretical and experimental results that link the properties of the heterointerface to the macroscopic mechanical behavior of metallic composites where the continuous phase is a metal and the hard phase is a ceramic (MMCs) or an intermetallic (IMCs). The results emphasize that the properties of the composites depend on the interaction between cohesive strength of the M/C or M/I interface and the physical microstructural scale of the metal. This result is general and is expected to apply from room temperature properties, such as toughness, to creep resistance at very high temperatures. At room temperature the effect of scale is based on the dislocation pile-up model for delamination at the interface. At high temperatures the climb rate of dislocations in the metal layer depends on its width and on the pinning efficiency of lattice dislocations at the interface.

Not For	
NTIS	DTIC
DTIC	DTIC
Unannounced	Unannounced
Justification	
By	
Distribution	
Availability Codes	
Dist	Avail and/or Special
A-1	

DTIC QUALITY INSPECTED 3

## 1. In-Situ Stress Strain Response of Small Metal Particles Embedded in a Ceramic Matrix

### 1.1 ABSTRACT

The *in-situ* stress-strain response of metal particles embedded in a ceramic matrix was obtained by combining the measurement and the modeling of the crack opening displacement field of a crack in a brittle material bridged by metal particles. The experiments were done on a composite made from platinum particles with a volume fraction of 10% in a magnesium aluminate spinel matrix. The size of the platinum particles was varied from 1 - 12  $\mu\text{m}$  to study the influence of scale on the deformation behavior. Large strain to failure and ultimate tensile strength of 550 MPa were obtained for the 1  $\mu\text{m}$  particles. But the larger particles failed at a strain of less than 25%; the ultimate tensile strength was also lower. This difference in ductility is explained in terms of debonding at the metal ceramic interface. It is argued that the debonding depends on the length of the dislocation pile up at the interface, and, therefore, on the particle size. The results and the metallographic observations are consistent with a model presented here; in this model the failure condition is given by a combination of the intrinsic yield stress of platinum, and the hydrostatic constraining stress in the metal particle.

### 1.2 INTRODUCTION

This study was undertaken to understand the significance of scale in the deformation of ductile particles functioning as toughening agents in a ceramic matrix through crack bridging. While there has been great discussion about the importance of constraint on deformation in large-scale, metal/ceramic composites, [1][2][3][4][5] the scale of the ductile component can also become an important factor in deformation behavior when the size of metal particles begins to approach the spacing between dislocations.

Historically, the effect of small dimensions upon deformation in metals has been demonstrated by Brenner<sup>[6]</sup> (1956) in experiments on the tensile strength of metal whiskers having a range of diameters. The tensile strength of copper whiskers, for example, increases substantially

---

<sup>1</sup>M. Bannister and M.F. Ashby, *Acta metall. mater.*, 39 [11], 2575-2582, (1991)

<sup>2</sup>A.R. Akisanya and N.A. Fleck, *Acta metall. mater.*, 41 [1], 121-131, (1993)

<sup>3</sup>M.F. Ashby, F.J. Blunt, and M. Bannister, *Acta metall. mater.*, 37 [7], 1847-1857, (1989)

<sup>4</sup>H.C. Cao, et al., *Acta metall. mater.*, 37 [11], 2969-2977, (1989)

<sup>5</sup>T.C. Lu, et al., *Acta metall. mater.*, 39 [8], 1853-1862, (1991)

<sup>6</sup>S.S. Brenner, *J. Appl. Phys.*, 27 [12], 1484-1491, (1956)

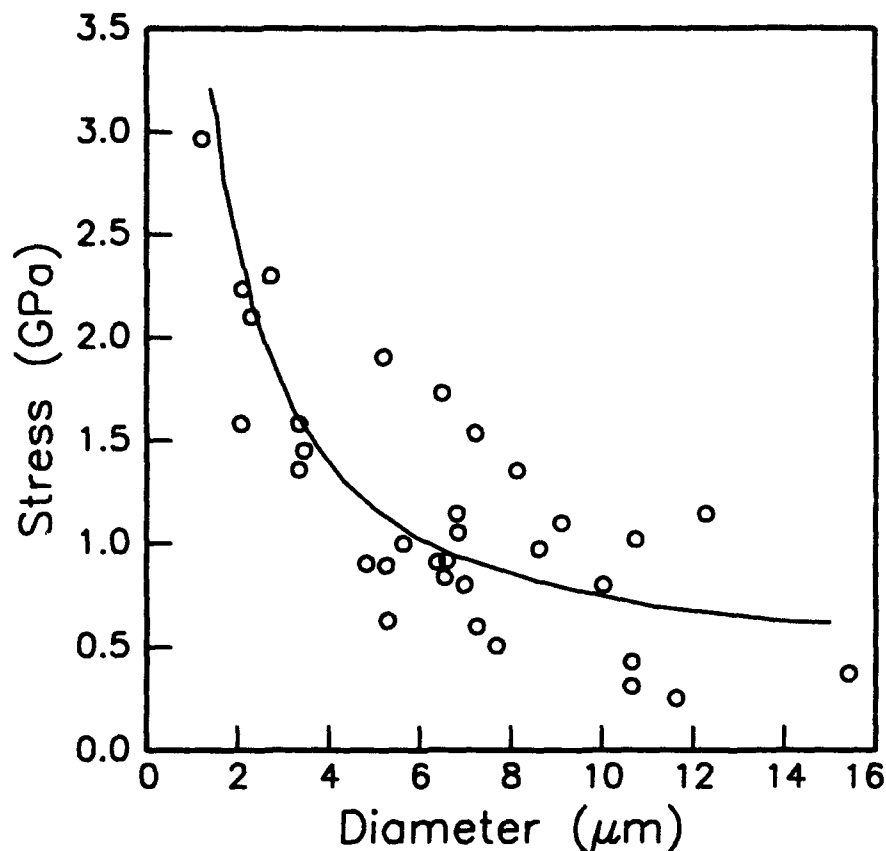


**Figure 1** The effect of size on the tensile strength of copper whiskers. (after Brenner [6]).

above bulk copper values when the diameter of the whisker is less than 10  $\mu\text{m}$ , as shown in Figure 1. The size/strength relationship in metal whiskers is attributed to the stress required to nucleate dislocations at surface steps.[7] As the diameter of the whiskers decreases, dislocation nucleation is more difficult due to energy considerations, thus increasing the tensile strength.

The *in-situ* stress-strain response of metals embedded in a ceramic matrix has thus far been measured only in large-scale, single metal fiber composites. The model composites studied consist of a single wire or plate of metal (approximately 1 mm in thickness) stressed in tension within a section of brittle matrix material that has been circumferentially cracked to initiate bridging.<sup>[1-5]</sup> These studies have demonstrated the influence that constraint has upon the deformation behavior of the ductile metal. In the case where bonding at the metal/ceramic interface is strong, the peak stress in the highly constrained wire generally reaches 4-8 times the yield strength of the bulk metal. When debonding at the interface occurs within the gauge section of the wire, causing constraint to be lower, the peak tensile

<sup>1</sup>A. Nohara, Jpn. J. Appl. Phys., 21 [9], 1287-1292, (1982)

stress decreases and the overall strain to failure of the wire increases. Such behavior is summarized in a sketch of stress-strain results obtained by Ashby, et al.<sup>[3]</sup> for the deformation behavior of 1 mm thick Pb wires embedded in a glass matrix, shown in Figure 2.

In light of the unique behavior of metals having dimensions on the order of the spacing of dislocations, the question now arises as to what influence the scale has upon the deformation behavior of constrained metal particles of 1  $\mu\text{m}$  diameter embedded in a ceramic matrix. We find that there is indeed an important scale effect, not only in the large peak stresses within the particles ( $18\sigma_0$ ), but also in the amount of deformation achieved within the bridging particle as a function of debonding. We believe that the small failure strains observed for larger particle sizes is related to a size-dependent debonding mechanism that initiates catastrophic failure of the metal/ceramic interface.

## 1.2 EXPERIMENTAL TECHNIQUE

Model metal/ceramic composites of 10 vol% platinum particles in an equimolar magnesium aluminate spinel matrix ( $\text{MgO} \cdot \text{Al}_2\text{O}_3$ ) were fabricated for this experiment via powder processing and hot-pressing techniques. Composite powders of the desired composition were produced by a solution method<sup>[8]</sup> in which  $\text{Mg}(\text{NO}_3)_2 \cdot 6\text{H}_2\text{O}$  was dissolved in distilled water at 70°C and platinum particles of the desired size and amount were added to the solution.  $\text{Al}(\text{OH})_3$  was then added in the appropriate ratio and the water was allowed to evaporate as the mixture was continuously stirred. The resulting powder was dried and then calcined at 700 °C in an alumina crucible for 90 minutes. The powder was then ground in an agate mortar and pestle.

Hot pressing of the composite powders was performed in a 1 cm graphite die lined with graphite foil. Two grams of powder were cold compacted and then hot pressed under a load of 83 MPa in a vacuum furnace ( $10^{-4}$  Torr) with graphite heating elements at 1600 °C for 30 minutes. The load was then released and the samples were allowed to cool slowly. The final pellet size was approximately 10 mm x 5 mm.

The three platinum/spinel composites were characterized using x-ray diffraction, fractographic analysis and microanalysis of the fracture surface. X-ray diffraction results showed that Pt and  $\text{MgAl}_2\text{O}_4$  were the only phases present in the composites. Similarly, electron microprobe studies of the fracture surface did not detect any foreign elements, interfacial reactions, or compositional differences in either the platinum or spinel regions for all three composites. Through fractographic analysis, the area fraction of platinum at the fracture surface (12%) was found to be only slightly higher than the bulk volume fraction. The average initial diameter of failed Pt ligaments was measured at the fracture plane of the matrix and found to be 1.3  $\mu\text{m}$ , 6  $\mu\text{m}$ , and 12  $\mu\text{m}$  for the small, medium, and large Pt-size composites, respectively.

Mechanical testing of the three composites was done using a technique for controlled crack growth in the SEM.<sup>[9]</sup> This technique was used to measure the crack-opening displacement profile of a loaded

---

<sup>a</sup>P.C. Panda, Ph.D. Thesis, Cornell University, (1984)

<sup>b</sup>D.S. Farquhar, Ph.D. Thesis, Cornell University, (1991)

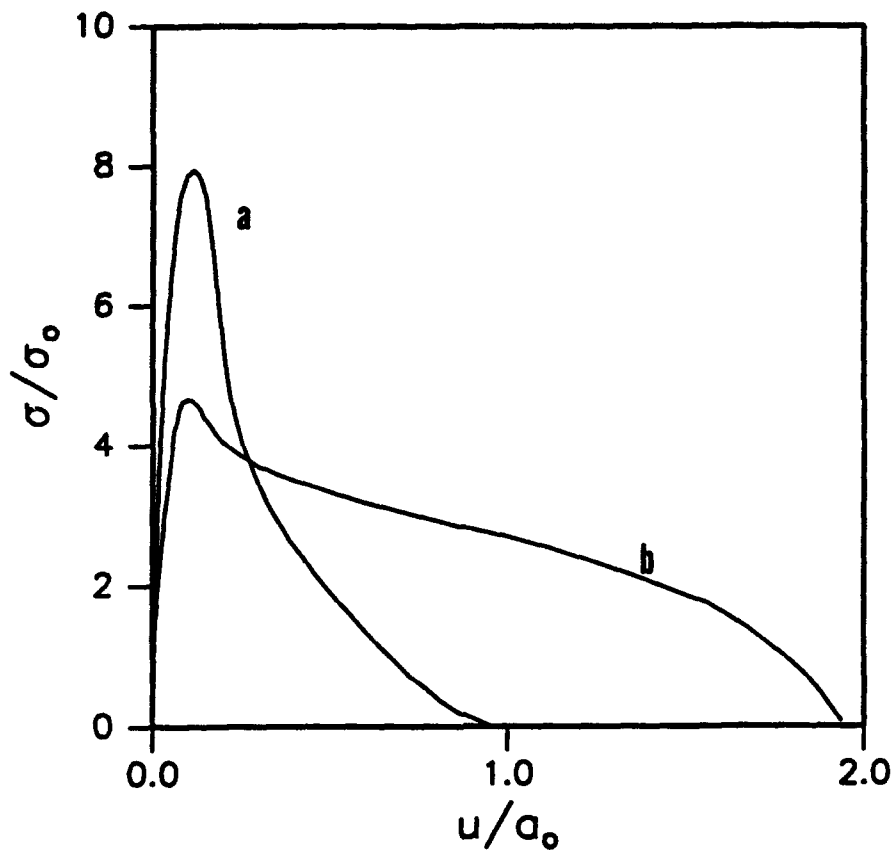


**Figure 2** Sketch of stress-strain results for Pb wires deforming in a glass matrix (Ashby, et al.[3]): (a) no debonding, full constraint; (b) some debonding, partial constraint.

crack in the Pt/spinel composites held just below the critical stage for crack growth. The brass fixture, shown schematically in Figure 3, acts as the side of a bending beam, creating a tensile stress that diminishes toward the neutral axis followed by a rising compressive stress, when loaded with a screw that pushes against one arm of the fixture. A thin section of the material to be tested is glued to the brass fixture, polished to a 0.05  $\mu\text{m}$  finish, and a crack is initiated at the upper tensile surface with a Vickers indenter. The crack is then extended to a stable length, the entire fixture is coated with Au-Pd to prevent charging in the SEM and the crack is extended just prior to placing the fixture in the SEM to insure a critical crack. The lengths of cracks examined in this study were approximately 2000-2800  $\mu\text{m}$ .

The crack opening displacement profile of a loaded crack in the Pt/spinel composites was recorded by locating the tip of the crack and taking a sequential series of photomicrographs from the tip to the end to the crack. Typical values for the initial measureable separation between the crack faces ranged from 30-80 nanometers. The photomicrographs were then pieced together to form a montage and the perpendicular distance between the faces of the crack was measured at intervals from the tip to obtain the crack-opening displacement vs. distance from the tip for each composite. Two example sections from a typical photomicrograph series are



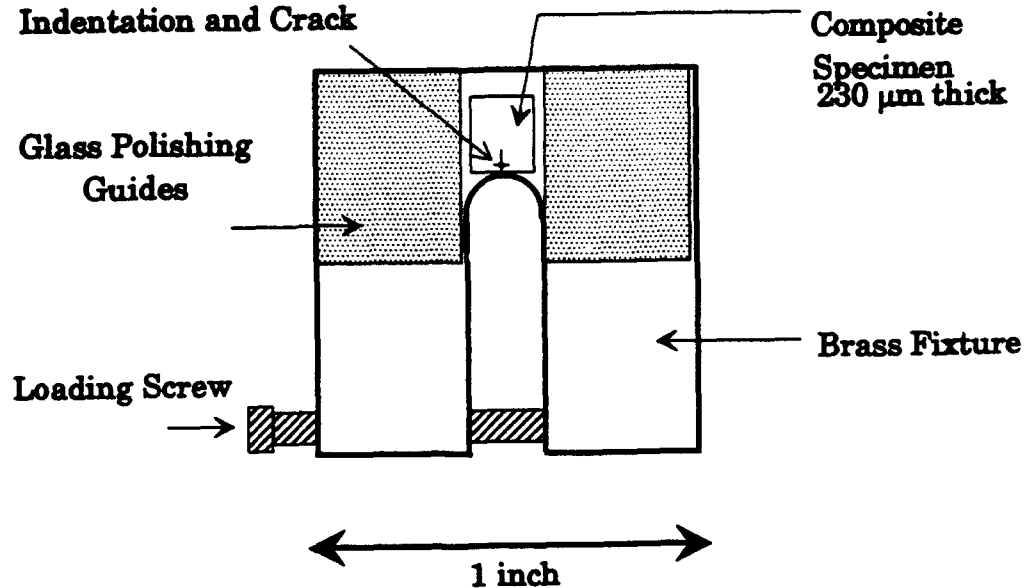


**Figure 3** Schematic of brass fixture used to measure the profile of a crack in the Pt/spinel composites held just below the critical stage for growth.

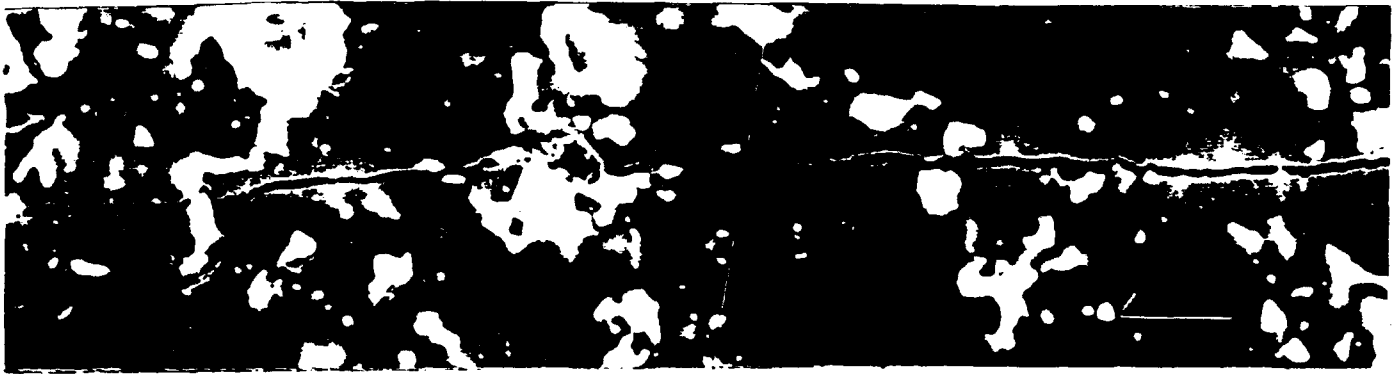
shown in Figure 4.

### 1.3. ANALYSIS OF THE TRACTION ON THE SURFACE OF THE BRIDGED CRACK

The stress-strain behavior of the platinum particles in the spinel matrix was obtained from the crack opening displacement data using a model for plane elasticity developed by McClintock, et al. [10]. In the McClintock model, the elastic behavior of a crack in an infinite body is simulated by superimposing pairs of dislocations and calculating the resulting stress and displacement fields of the dislocation pairs. The crack is thus modeled as a series of segments, bounded by dislocations, where traction and displacement for each segment are reported at the midpoint.

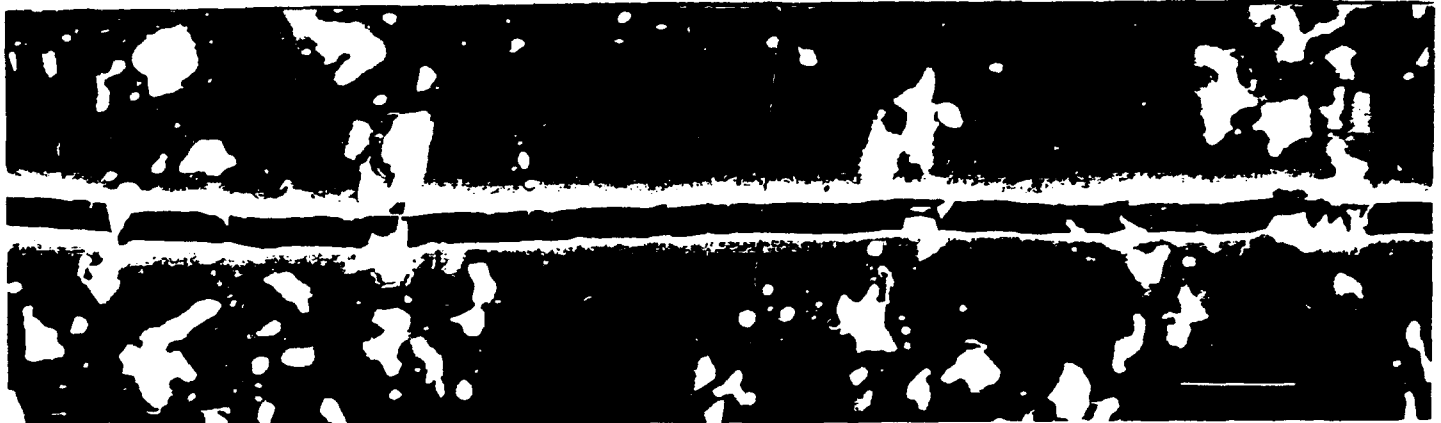
The model is used by first establishing the typology of the crack under consideration. The total length of the crack, the number of segments describing it, and the length of each segment must be specified. The material constants of modulus,  $E$ , and Poisson's ratio,  $\nu$ , are then

<sup>10</sup>F.A. McClintock, et al., Research Memorandum No. 177R2. Fatigue and Plasticity Laboratory, MIT (1974)



150  $\mu\text{m}$  from tip

Nearing end of bridging zone.



1100  $\mu\text{m}$  from tip

Far beyond bridging zone.

**Figure 4** Example sections from photomicrograph series recording the COD profile of a crack in a 10 vol%, 1  $\mu\text{m}$ -Pt/spinel composite.

given along with the stress applied to the body at infinity,  $\sigma_\infty$ . The appropriate boundary conditions are specified for each segment of the crack. For the problem at hand, a displacement is imposed on each segment (e.g. crack opening profile). The model then calculates the bridging tractions acting on each segment.

The results of the model were verified against the classic Dugdale crack in which a constant closing force acts along the bridging zone. When the displacement profile of the Dugdale crack is specified as boundary conditions, the McClintock model returns a constant traction (equal to the bridging stress in the Dugdale solution) for segments within the zone of bridging. Traction falls to zero for segments outside the zone. The resulting bridging stress varies along the length of the crack as shown in Figure 5.

The average closing forces exerted by ductile particles in a ceramic matrix may be determined using the McClintock model in a similar manner.

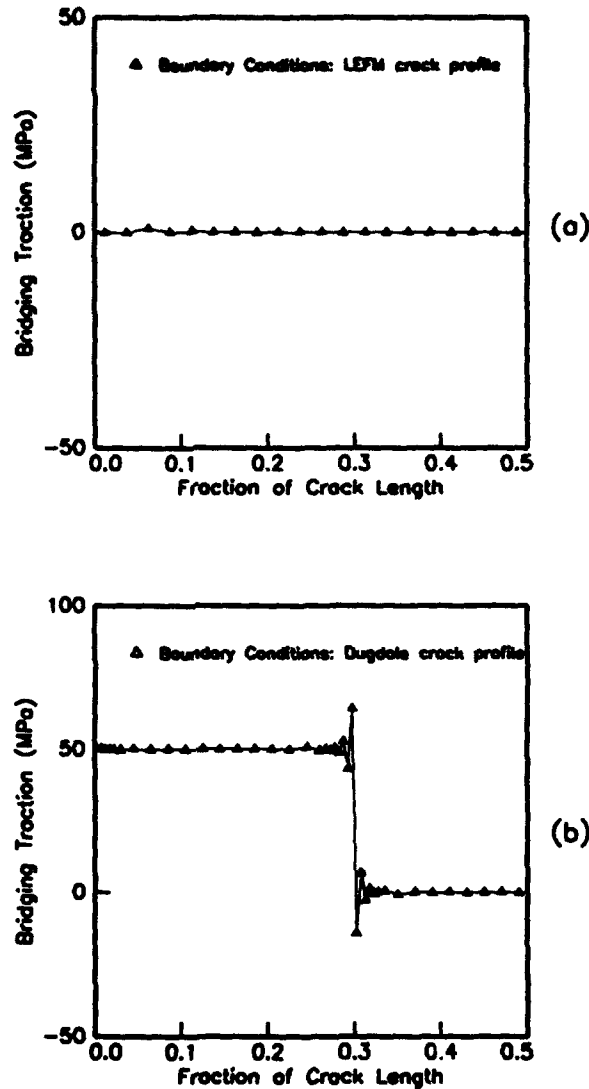


**Figure 5** Bridging tractions calculated by the McClintock model for boundary conditions of: (a) COD profile of unbridged crack; (b) COD profile of Dugdale crack bridged for 30% of its length.

When the experimentally measured crack opening profile for the composite is specified as the boundary conditions of displacement, the model calculates the average tractions acting on the crack faces as a function of distance from the tip. Since these tractions are not found for a pure, brittle material, the calculated tractions are a result of the average closing forces exerted by the particles along the zone of bridging that develops in the wake of the crack.

Although the applied stress,  $\sigma_w$ , is not known in the controlled

crack growth technique used to measure the displacement profiles, we do know, however, that the bridging zone ends at some arbitrary distance from the crack tip and that the tractions on segments falling beyond that zone must be zero. Calibrations performed on the Dugdale crack profile showed that a value of applied stress set deliberately high in the model yielded a set of tractions that did not fall to zero. If the value of applied stress was set deliberately low, the tractions progressed from tensile to zero to compressive stresses. Thus, the applied stress was determined in an iterative manner for each crack profile by adjusting its value in the model until tractions become zero at an arbitrary distance from the tip and do not become compressive. An illustration of the technique is shown in Figure 6.

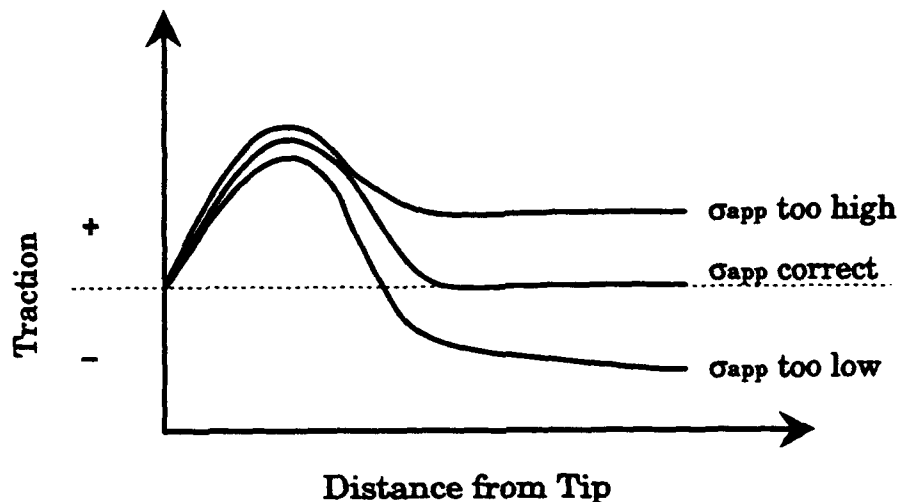


**Figure 6** Method used to determine the applied stress in the McClintock model.

The calculated traction vs. distance from the tip is then converted to the stress-strain response of the average bridging particle in the following manner. When the traction on each segment is divided by the area fraction of ductile particles at the fracture surface, the bridging stress in the average particle is then known as a function of distance from the crack tip. The values obtained for each segment of the crack correspond to sequential stages of tensile deformation for an average sized particle in the brittle matrix. Stress vs. strain is then obtained by dividing the corresponding crack opening displacement for each segment by the average initial radius of the ductile particles.

#### 1.4. RESULTS

The experimentally obtained crack opening profiles for cracks in the 10 vol% Pt/spinel composites having average Pt ligament diameters of 1.3  $\mu\text{m}$ , 6  $\mu\text{m}$ , and 12  $\mu\text{m}$  are shown in Figure 7. In each case, an upper and a

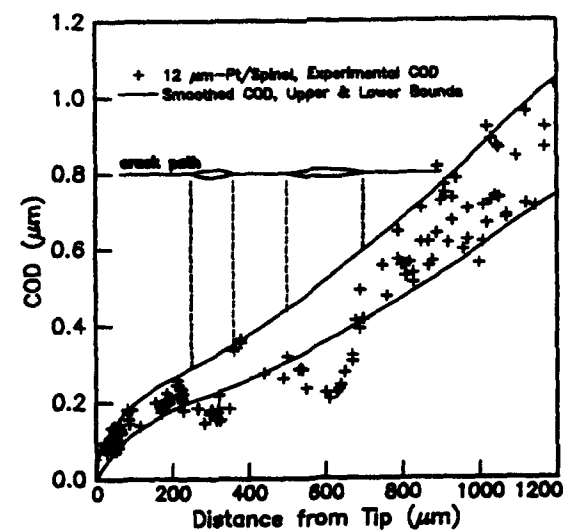
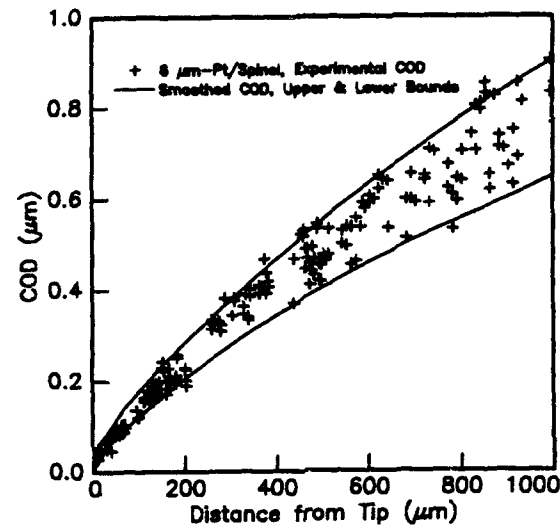
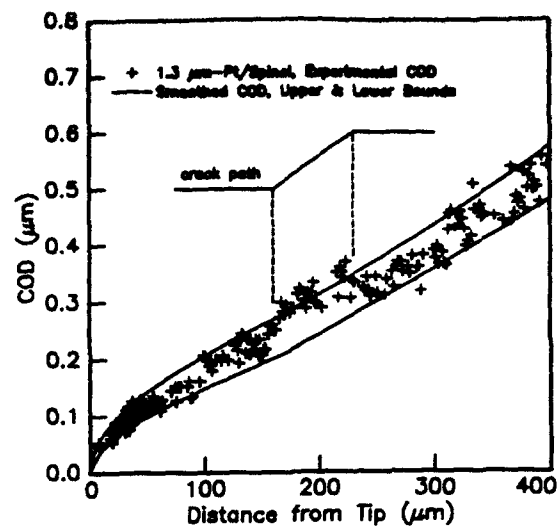


**Figure 7** Measured COD profiles for cracks in composites of 10 vol% Pt in spinel, having average Pt ligament diameters of 1.3 μm, 6 μm, and 12 μm.

lower limit of displacement are shown. These smoothed profiles were applied as boundary conditions in the McClintock model to obtain the upper and lower bounds of the in-situ stress-strain response for each particle size. Deviations from linearity in the path of the crack and regions of crack bifurcation can be seen in the displacement profiles where noted.

An example is shown in Figure 8 of bridging tractions obtained for a pure spinel sample and for the lower displacement limit of a 1  $\mu\text{m}$ -Pt/spinel particulate composite. As expected, the average bridging tractions are zero in the pure spinel sample, and a zone of bridging in the platinum/spinel composite is indicated by non-zero, average bridging tractions.

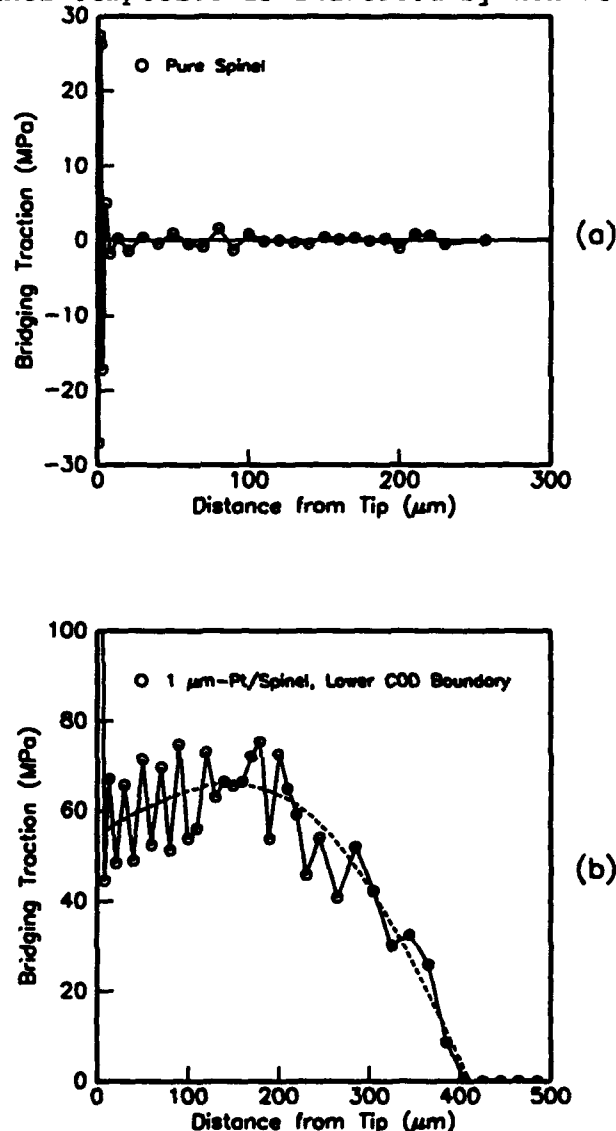


**Figure 8** Bridging tractions acting on the surfaces of a crack in (a) pure spinel, and (b) 10 vol% 1  $\mu\text{m}$ -Pt/spinel composite.

The upper and lower limits of the in-situ stress-strain response for three sizes of platinum particles in spinel are shown in Figure 9. The

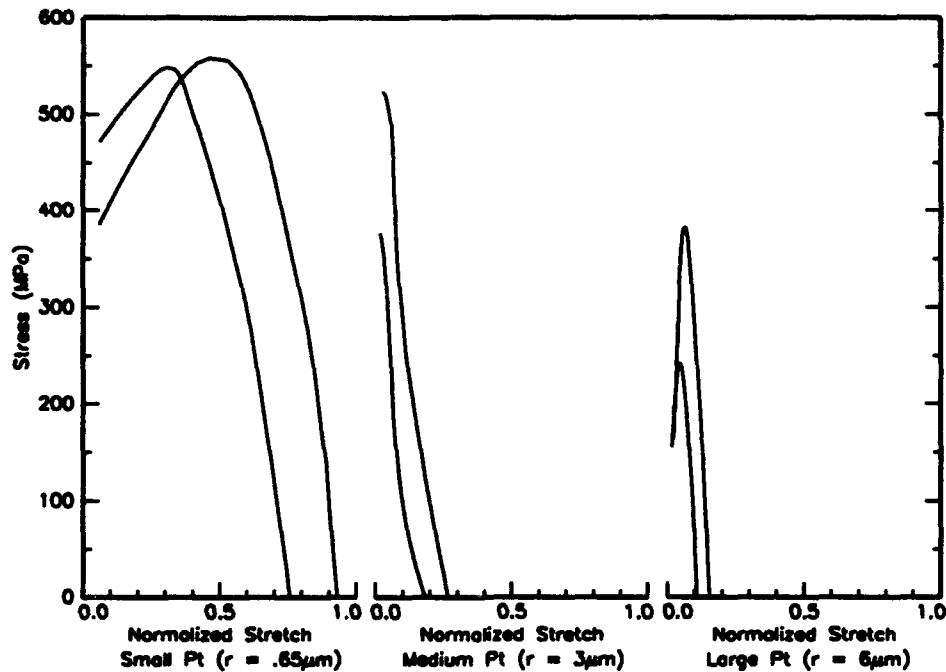


**Figure 9** Upper and lower stress-strain limits for three sizes of platinum particles in spinel.  $r$  is the average bridging ligament radius, and Normalized Stretch = COD/ $r$ .

maximum bridging stresses observed are 550 MPa, 450 MPa, and 300 MPa for the Pt particle sizes of 1.3  $\mu\text{m}$ , 6  $\mu\text{m}$ , and 12  $\mu\text{m}$ , respectively. The decrease in the maximum stress with increasing particle size is consistent with both constraint and scale considerations. Larger particles inherently experience less constraint, and hence exhibit a lower stress. From previously discussed experiments on metal whiskers, notable decreases in the maximum stress are also expected when the diameter of the particle exceeds approximately 10  $\mu\text{m}$ . Finally, the magnitude of maximum stress in the 1.3  $\mu\text{m}$  Pt particles (550 MPa) is consistent with thin film literature values for highly constrained metals deforming on the micron

scale.[11]

The strength of the Pt/spinel interface plays a very important role in the strain to failure achieved in each composite. Experimental evidence accrued from many points of view supports the premise that bonding between the Pt particles and the spinel matrix was initially strong in all three composites. Despite uniform processing conditions, the absence of any detectable chemical differences between the composites, and very high initial stresses that indicate strong initial Pt/spinel bonding in all three cases, the medium and large size Pt particles reach bridging failure at strikingly lower strains than in the small Pt case.

Examination of the fracture surface of the composites revealed that the small Pt particles remained well bonded to the matrix and ultimately necked down to tensile failure as shown in Figure 10. This behavior is in agreement with the large strain to failure (85%) obtained for the stress-strain response of 1.3  $\mu\text{m}$  Pt in spinel.



**Figure 10** SEM photomicrograph of small platinum particles deformed in a spinel matrix. Particles remain well bonded to the matrix and fail by necking.

The composites having 6  $\mu\text{m}$  and 12  $\mu\text{m}$  Pt particles behaved quite differently. Rapid decreases in bridging stress and small strains to failure were caused by catastrophic debonding and pull-out of the Pt particles from the spinel matrix after only small amounts of deformation. Photomicrographs of the large particles, shown in Figure 11, reveal extensive debonding at the base of the particles, impressions of spinel

---

<sup>11</sup>M.A. Korhonen, P. Børgesen, and C.-Y. Li, Reliability Issues in Microelectronics, Mater. Res. Soc. Proc. 225, Pittsburgh, PA, 133-142, (1991)



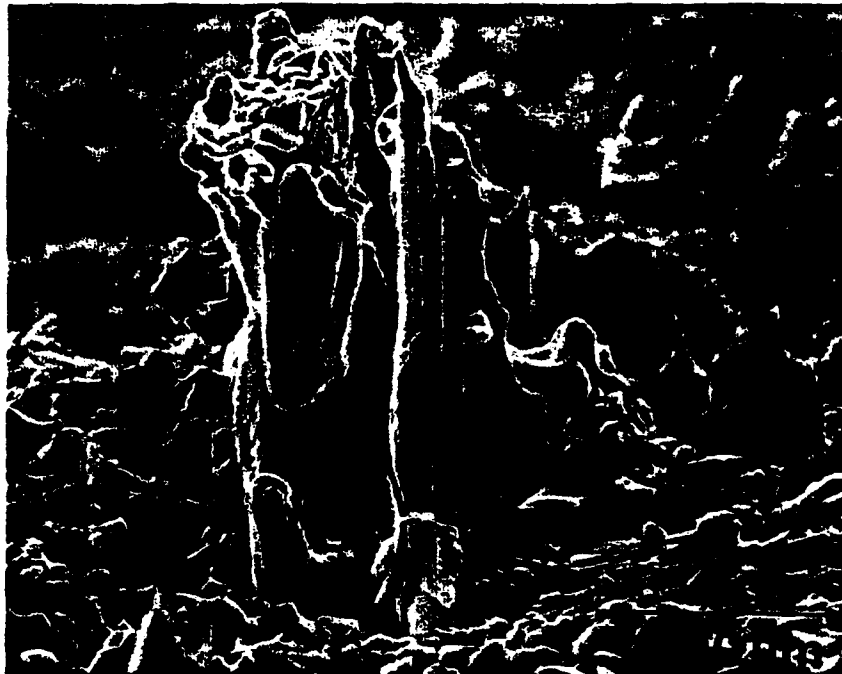


**Figure 11** SEM photomicrographs of large platinum particles deformed in a matrix of spinel. Small strains, debonding, and vertical scoring during pull-out are evident.

grains on the surface of the particles, and scoring tracks left by the spinel grains as the upper half of the matrix pulled away from the particles.

## 1.5 DEBONDING AT THE METAL-CERAMIC INTERFACE

The mechanism that controls catastrophic debonding was inactive in the small-Pt/spinel composite during the entire deformation process. In the medium and large-Pt composites, however, a mechanism was activated some time during deformation that caused total Pt/spinel interface failure. The mechanism we propose to explain this behavior is based on the force exerted by dislocation pile-ups at a metal/ceramic interface.

The stress acting on the head of the pile-up is a multiple of the applied stress and the number of dislocations in the group. The number of dislocations is limited by the maximum pile-up length, which, in the case of ductile particles in a brittle matrix, is proportional to the diameter of the micron-scale particle for a given magnitude of the plastic strain. When the pile-up is sufficiently long, the high stresses at the metal/ceramic interface may be relieved by nucleation of microcracks within the interface, ultimately causing adhesion failure between the particle and the matrix. Whether or not such a failure mechanism would be active is dependent upon the size of the metal particle and the strength of the interface.

A situation analogous to dislocation pile-up at metal/ceramic interfaces is found in the formation of internal cracks resulting from plastic flow in ductile materials. It is instructive, therefore, to examine the conditions for dislocation-induced cracking in metals. Mott[12] and Stroh[13][14] considered the formation of cracks in metals when dislocations are piled up against some type of internal barrier, such as a grain boundary. Their theories demonstrated that the stress concentration at the head of a dislocation pile-up may be sufficient to nucleate a wedge crack at the barrier. Cottrell[15] analyzed the formation of cleavage cracks in metals where dislocations, operating on intersecting slip planes 45° to the tensile axis, coalesce to form a superdislocation equivalent to a cleavage crack that is oriented perpendicular to the externally applied stress. Cottrell's analysis followed an expression given by Stroh<sup>[14]</sup> for the total energy of the crack, but included the influence of both the effective shear stress acting on the dislocations in the slip planes and the applied tension stress acting normal to the crack opening. The end result of his analysis is an expression for the equilibrium between a stable crack of finite size and a cleavage crack growing indefinitely, as given by:

$$pnb = 2\gamma \quad (1)$$

where  $p$  is the applied tension stress,  $b$  is the Burgers vector,  $n$  is the number of dislocations that have coalesced to form the crack, and  $\gamma$  is the

---

<sup>12</sup>N. F. Mott, Proc. Roy. Soc. A, 220, 1, (1953)

<sup>13</sup>A.N. Stroh, Proc. Roy. Soc. A, 223, 404, (1954)

<sup>14</sup>A.N. Stroh, Advances in Physics, 6 [21-24], 418-465, (1957)

<sup>15</sup>A.H. Cottrell, AIME Trans., 212, 192-203, (1958)

surface energy of the metal. Using the Eshelby-Frank-Nabarro[16] expression to estimate the number of piled up dislocations that can occupy a distance  $d$  along a slip plane:

$$nb = \frac{\pi(1-\nu)\tau_{eff}d}{G} \quad (2)$$

where  $G$  and  $\nu$  are the shear modulus and Poisson's ratio of the metal and  $\tau_{eff}$  is the effective shear stress, or the difference between the applied shear stress acting on the dislocation and the lattice friction stress that retards their motion, Eqn (1) can then be expressed in terms of the pile-up length and the acting shear stress:

$$\frac{p\pi(1-\nu)(\tau-\tau_i)d}{2G} = \gamma \quad (3)$$

Eqn (3) is a fracture criterion based on the surface energy of the fracturing material, the potential length of dislocation pile-up, and the stress acting in the material, where  $\tau$  is the shear stress acting on the slip plane,  $\tau_i$  is taken to be the Peierls stress, and  $p$  is the applied tensile stress acting on the crack.

With slight modification, Cottrell's fracture criterion can be used to estimate whether or not the potential pile-up length in a micron-scale ductile particle is sufficient to nucleate and grow microcracks at the metal/ceramic interface when the stress in the particle is known. We will assume that the bonding was initially strong in all three composites, and that debonding was initiated after plastic deformation had occurred. We also assume that the Pt/spinel interface fails in a 'brittle' manner in the large particle size composites, as previously shown micrographs indicate very little ductile rupture of the interface. Finally, we assume that the crack opening stress,  $p$ , under conditions of uniaxial stress in Cottrell's model is equivalent to the dilatational (or hydrostatic) component of stress in the triaxially loaded particles.

The general expression for the hydrostatic stress component is given in terms of the principal stresses by:

$$p = \sigma_{mean} = \frac{\sigma_1 + \sigma_2 + \sigma_3}{3} \quad (4)$$

For the case of ductile particles embedded in a constraining matrix,  $\sigma_1$  corresponds to the maximum tensile stress within the particle, measured in the current study as the peak stress of the stress-strain response for the average bridging particle.  $\sigma_2$  and  $\sigma_3$  arise from the constraint of the surrounding matrix and are equal, but unknown. This value, however, can be estimated from the equations for elasticity assuming total constraint. Thus, an upper bound on  $\sigma_2$  is given in terms of the known tensile stress:

The mean stress and the maximum shear stress then become:

---

<sup>16</sup>J.D. Eshelby, F.C. Frank, and F.K.N. Nabarro, Philos. Mag., 42, 295-302, (1959)

$$\sigma_2 = \sigma_3 = \left( \frac{v}{1-v} \right) \sigma_1 \quad (5)$$

$$p = \sigma_{mean} = \frac{\sigma_1 + \sigma_2 + \sigma_3}{3} = \frac{\sigma_1}{3} \left( 1 + \frac{2v}{1-v} \right) \quad (6)$$

$$\tau = \tau_{max} = \frac{\sigma_1 - \sigma_2}{2} = \frac{\sigma_1}{2} \left( 1 - \frac{v}{1-v} \right) \quad (7)$$

Substituting these expressions into Eqn (3), the conditions for dislocation induced debonding of ductile inclusions in a ceramic matrix are given by:

$$\frac{\frac{\sigma_1}{3} \left( 1 + \frac{2v}{1-v} \right) \pi (1-v) \left[ \frac{\sigma_1}{2} \left( 1 - \frac{v}{1-v} \right) - \tau_{Poirierls} \right] d}{2G} = \Gamma_{M/C} \quad (8)$$

where the pile-up length  $d$  is taken as the radius of the ductile inclusion,  $G$  is the shear modulus of the inclusion, and  $\sigma_1$  is the maximum in the tensile stress-strain curve for the average ductile particle. The right hand side of Eqn (8) is the equivalent of  $\gamma$  in Cottrell's derivation, but for the case of a metal surface and a ceramic surface being created at the expense of a metal/ceramic interface. Thus,  $\gamma$  in Eqn (3) is replaced by  $\Gamma_{M/C}$  where:

$$\Gamma_{M/C} = [\gamma_M + \gamma_C - \gamma_{M/C}] / 2 \quad (9)$$

Here  $\gamma_M$  is the surface energy of the metal component,  $\gamma_C$  is the surface energy of the ceramic component, and  $\gamma_{M/C}$  is the energy of the metal/ceramic interface. Although the energy of the platinum/spinel interface,  $\gamma_{Pt/spinel}$ , is not readily available in the literature, its value was estimated from observations of contact angles for platinum beads that had grown on the polished surface of a 10 vol% Pt/spinel composite via vapor transport during annealing. From the observed contact angle ( $75^\circ \pm 5^\circ$ ), the energy of the platinum/spinel interface was estimated to be  $0.5 - 0.7 \text{ J/m}^2$ .

The criterion for dislocation pile-up induced debonding at of ductile particles in a brittle matrix, given in Eqn (8), was evaluated using the measured parameters for each of the small, medium, and large-Pt/spinel composites. Catastrophic debonding is predicted by this model when the left side of Eqn (8) exceeds the right side using the estimated energy of the Pt/spinel interface discussed above. A summary of the measured and estimated parameters used is given in Table I, along with the results of the model for each of the three Pt/spinel composites studied. The model predicts no growth of interface microcracks in the case of small Pt particles embedded in a ceramic matrix. This is in agreement with the stress-strain results obtained for this composite and with observations of failed particles on the fracture surface which remain well bonded to the matrix and fail in a fully ductile manner. While less distinct, the model also predicts growth of microcracks at the interface for the case of

medium and large Pt particles in spinel. In both composites, catastrophic failure of the interface was observed directly on the fracture surface of the composite and indirectly in the measured stress-strain response of the inclusions.

## 1.6 SUMMARY

A method for determining the in-situ stress-strain response of ductile particles in a brittle matrix was presented in this study. The average stress-strain curves were then measured for 1.3  $\mu\text{m}$ , 6  $\mu\text{m}$ , and 12  $\mu\text{m}$  platinum particles bridging a crack in a spinel matrix. An ultimate tensile strength of 550 MPa and strain to failure of 85% were observed in the 1.3  $\mu\text{m}$  particles. The maximum stress was found to decrease with increasing particle size.

A particle size dependent debonding phenomenon was observed in the composites as the small platinum particles remained well bonded to the matrix and failed in a ductile manner, while the medium and large platinum particles experienced catastrophic debonding after small amounts of plastic deformation. A model was proposed to explain this behavior based on dislocation pile-up induced debonding at metal/ceramic interfaces. The

**Table I:** Predicting size-dependent debonding : Summary of values used and results of model (Eqn 8).

	<u>Small-Pt/spinel</u>	<u>Medium-Pt/spinel</u>	<u>Large-Pt/spinel</u>
$\sigma_1$	550 MPa	450 MPa	300 MPa
$\nu$	0.39	0.39	0.39
$d$	1 $\mu\text{m}$	4.7 $\mu\text{m}$	9.4 $\mu\text{m}$
$\tau_{\text{Peters}}$	0.6-6 MPa	0.6-6 MPa	0.6-6 MPa
Eqn 8 (left side)	0.61-0.65 J/m <sup>2</sup>	1.9-2.0 J/m <sup>2</sup>	1.6-1.8 J/m <sup>2</sup>
$\Gamma_{\text{Pt/spinel}}$	1.1-1.3 J/m <sup>2</sup>	1.1-1.3 J/m <sup>2</sup>	1.1-1.3 J/m <sup>2</sup>
Debonding predicted by model	not likely	yes	yes
Debonding observed	no	yes	yes

model was then evaluated using measured parameters from the composites and was found to agree with the fractographic and stress-strain behavior observed for platinum particles in a spinel matrix.

It is interesting to note that while debonding is required to achieve ductility of the bridging component in large-scale metal fiber/ceramic composites, debonding can easily be a catastrophic event in small-scale metal particle/ceramic composites. The particle size dependent phenomenon observed in these composites is highly dependent on the hydrostatic stresses achieved during constrained deformation. The mechanism would not operate in a large-scale metal/ceramic composite, despite longer pile-up lengths, since the hydrostatic component of stress drops rapidly as the scale increases. There is likely to be a very narrow window of particle sizes (e.g. 5-20  $\mu\text{m}$ ) for which this might occur.

## 2. The Influence of Microstructural Scale On Toughening of Metallic Composites.

### 2.1 ABSTRACT

We discuss the toughening achieved in a broad range of metal/ceramic composite systems as a function of the size of the ductile bridging constituent. For composites having discrete ductile particles or interconnected ductile networks, unusually large amounts of toughening occur when the dimension of the ductile member is very small. The work of plastic deformation is shown to be an inverse function of particle size for diameters on the micron scale.

### 2.1 METALLIC COMPOSITES OF DIFFERENT MICROSTRUCTURAL SCALE

**2.1.1 Large Scale Metal/Ceramic Composites:** The relationship between the toughness of a metal/ceramic composite and the microstructural parameters, namely, the volume fraction,  $V_f$ , and size scale,  $a_0$ , of the ductile component:

$$\Delta G_c = \frac{(1-v_c^2)K_c^2}{E_c} - \frac{(1-v_m^2)K_m^2}{E_m} = V_f a_0 \int_0^{u'/a_0} \sigma(u/a_0) d(u/a_0) \quad (10)$$

Here,  $c$  denotes composite values,  $m$  denotes matrix values, and the integral represents the work done to plastically deform the average bridging ligament to failure. This quantity is expressed in  $\text{J/m}^3$  and is given by the area under the stress-strain curve for the average ligament. The approximation in Eqn (10) could be rigorously eliminated by subtracting  $V_f G_m$  from the right-hand side. This term accounts for the reduction in the area of fractured matrix material due to the presence of the ductile phase. Since this term is usually small, the approximation in Eqn (10) is a good one and will be used in the following discussion.

A cursory examination of Eqn (10) suggests that the greatest toughening is obtained in composites having ductile inclusions of high

strength and large diameter. However, the effect of scale on the work of plastic deformation must also be considered. Studies of composite cylinders with ductile wires on the mm-scale have shown that the work of rupture increases linearly with the debond length ( $L_d/a_0$ ) for the metal fiber, as shown in Figure 12.<sup>[10]</sup> As the interfacial constraint relaxes and the debond length become larger, the gauge length for plastic deformation increases and a corresponding increase in the work of rupture occurs. Moderate debonding is a requirement to achieve considerable toughening in these large-scale ductile phase/brittle phase composites.

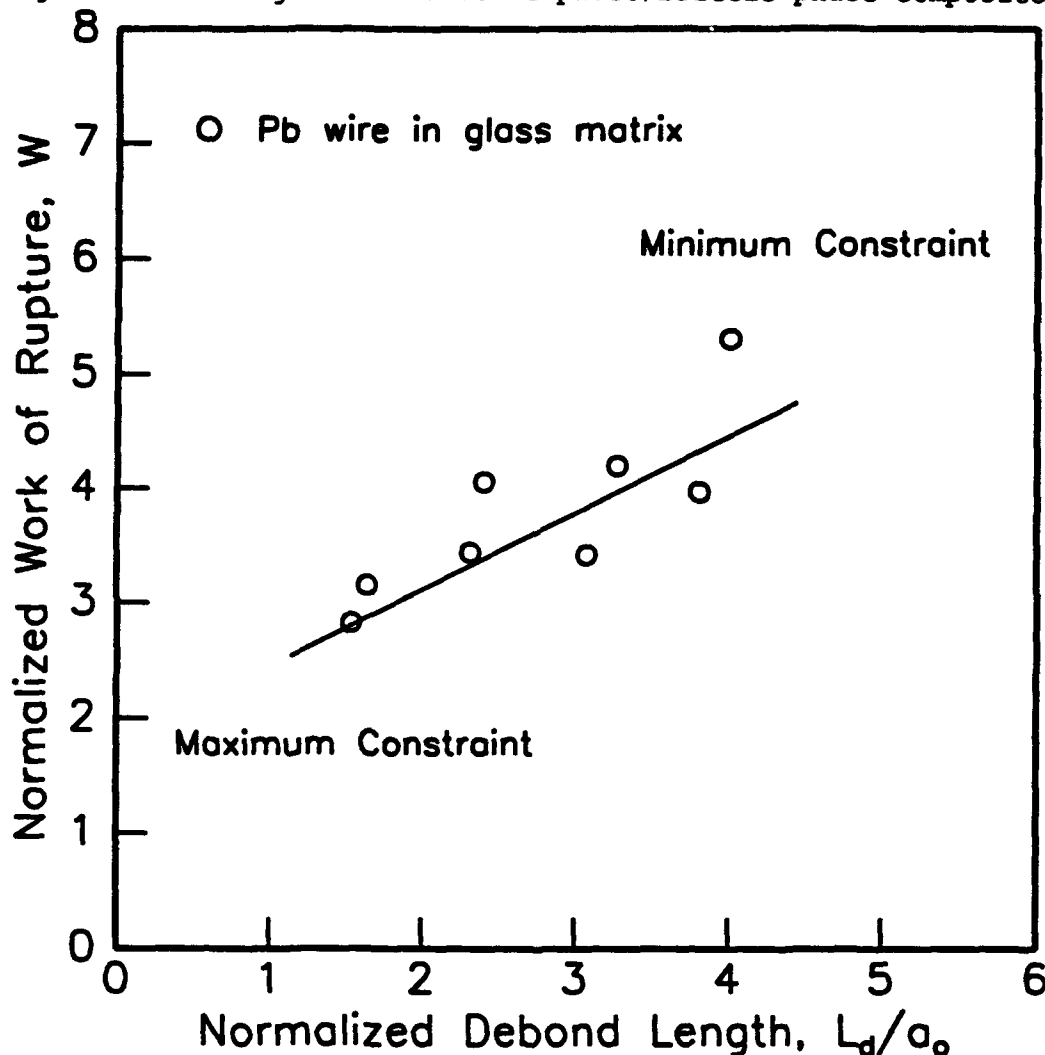


**Figure 12:** The effect of normalized debond length  $L_d/a_0$  upon the work of rupture parameter,  $W$ , for composite cylinder tests.<sup>[10]</sup>  $a_0 = 2$  mm.

**2.1.1 Types of Small Scale Metal/Ceramic Composites:** Small-scale, metal/ceramic composites shall be defined as those in which the effective radii of the ductile constituents range from sub-micron to a few hundred microns in dimension. When the ductile phase is less than 10  $\mu\text{m}$  in

diameter, the composites demonstrate unusual properties and will be referred to as "micron-scale" composites. Using Eqn (10), the toughening,  $\Delta G$ , and the work of deformation,  $U = \Delta G/V_f a_o$ , have been surveyed for a wide variety of small scale metal/ ceramic composites and are presented in Table II as a function of the scale parameter,  $a_o$ . Except where noted in Table II, the appropriate scale parameter for the composites is the radius of ductile particle or thickness of interconnected metal layer.

The composites of Table II fall into 4 geometric categories:

- Type I: discrete ductile particles in a brittle matrix;
- Type II: liquid phase sintered network of ductile phase in a brittle matrix;
- Type III: ductile fibers in a brittle matrix; and,
- Type IV: laminate of alternating layers of ductile and brittle materials.

A schematic for each of the 4 composite geometries is shown in Figure 13. The Type I particulate composites (# 8, 9, 15-17, 21-28) are similar to the Pt/ spinel composites of the study presented in Section 1. Here the scale parameter equal to the ductile particle radius. Composites 22, 26, and 28 are slightly different in that large Mo or Nb particles are embedded in a cemented carbide matrix rather than a purely ceramic matrix. The effective  $V_f$  of plastically deformed material for Type I composites is the bulk volume fraction of the ductile phase. Although Composite 17 is hotpressed above the melting point of Al, the low volume fraction metallic phase seems to be particulate in nature, rather than interconnected. This composite will also be considered as Type I in the subsequent discussion.

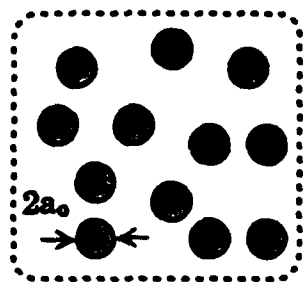
The Type II networked composites (# 1-7, 10-14, 18-20) consist mostly of tungsten or titanium carbides in a ductile binder of Co or Ru. These composites are fabricated by liquid phase sintering, which leaves a thin, usually continuous layer of binder phase surrounding matrix material grains. One special case is that of Composite 20, where the metal layer is formed by the Lanxide™ process. The appropriate scale parameter in Type II composites is the half-thickness of the metal layer, which is calculated from the linear-intercept size of the carbide grains,  $d$ , and the volume fraction of ductile binder,  $f$ , using:  
 $2a_o = f d / (1-f)$ . [17] The bulk volume fraction of the binder is noted in Table II for each composite. Since the path of a crack in these composites may strongly favor the metal/ceramic interface, the effective volume fraction of ductile material intercepting the crack may be taken as 1.

Type III fibrous composites are represented in Table II by a composite of W-3Re fibers in a TiTaAl matrix (# 29). Also included in this category are the composite cylinder (# 32, 33), or composite laminate (# 30, 34, 35) samples where a single wire or slab of metal is tested in tension in a pre-cracked matrix. The scale parameter in this case is half of the total debond length for the ductile fibers or slab. When multi-

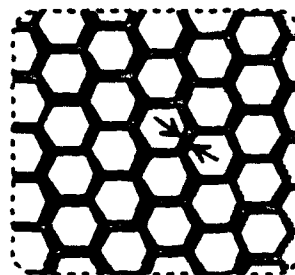
---

<sup>17</sup>Development and present status of the science and technology of hard materials., H.F. Fischmeister, Science of Hard Metals, Ed. R.K. Viswanadham, D.J. Rowcliffe, and J. Gurland, p. 1, (1983)

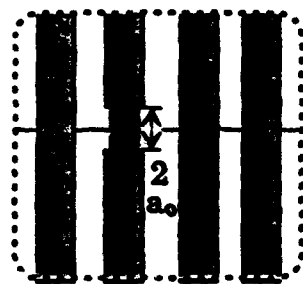




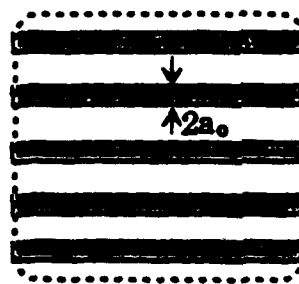
Type I: Particulate



Type II: Networked



Type III: Fibrous



Type IV: Laminate

Figure 13: The four composite geometries found in Table II.

THIS  
PAGE  
IS  
MISSING  
IN  
ORIGINAL  
DOCUMENT

Table II: Composite toughening vs. ductile constituent radius for a broad range of metal/ceramic composites.

(ID) Type	M/C [ref.]	$K_{IC} / K_I$ (MPa $\sqrt{m}$ )	$\nu_m / \nu_c$	$E_m / E_c$ (GPa)	$V_{t, bulk} / V_{t, eff}$	$a_c$ ( $\mu m$ )	$\Delta G$ (J/m $^2$ )	$\Delta G / V_{t, eff} a_c = U$ (MJ/m $^3$ )	Comments
(1) II	Co/WC [76]	7/8.3	.21 .26	690/640	.11 1	.04	32	800	Liq. phase sintered cemented carbide
(2) II	Co/WC [76]	7/8.6	.21 .23	690/600	.16 1	.05	49	980	"
(3) II	Co/WC [76]	7/10.6	.21 .26	690/650	.10 1	.09	93	1033	"
(4) II	Co/WC [76]	7/13.5	.21 .22	690/530	.26 1	.13	259	1992	"
(5) II	Ru/TiC [77]	5/7	.2 .21	450/446	.20 1	.13	52	477	"
(6) II	Co/WC [76]	7/12.8	.21 .26	690/650	.10 1	.20	167	835	"
(7) II	Co/WC [76]	7/12.8	.21 .22	690/515	.29 1	.20	235	1175	"
(8) I	Ni/Al $_2$ O $_3$ [39]	2.7/2.9	.2 .2	350/347	.02 .02	.20	3.3	825	Hotpressed, 1700C NiO reduced to Ni

Table II. (Continued)

(ID) Type	M/C [ref.]	$K_m / K_c$ (MPa√m)	$v_m$ $v_c$	$E_m / E_c$ (GPa)	$V_{f,bulk}$ $V_{f,eff}$	$a_c$ (μm)	$\Delta G$ (J/m <sup>2</sup> )	$\Delta G/V_{f,eff} a_c =$ U (MJ/m <sup>3</sup> )	Comments
(9) I	Ni/Al <sub>2</sub> O <sub>3</sub> [39]	2.7/3.8	.2 .21	350/342	.06 .06	.25	20	1333	Hotpressed, 1700C NiO reduced to Ni
(10) II	Co/WC [76]	7/15.1	.21 .22	690/540	.22 1	.29	334	1152	Liq. phase sintered cemented carbide
(11) II	Co/WC [76]	7/12.7	.21 .23	690/600	.16 1	.30	187	623	"
(12) II	Co/WC [76]	7/15.6	.21 .26	690/650	.10 1	.42	281	669	"
(13) II	Co/WC [76]	7/15.1	.21 .23	690/600	.16 1	.49	292	596	"
(14) II	Co/WC [76]	7/17.2	.21 .22	690/550	.21 1	.53	444	837	"
(15) I	Ni/Al <sub>2</sub> O <sub>3</sub> [39]	2.7/5	.2 .21	350/332	.13 .13	.60	52	667	Hotpressed, 1700C NiO reduced to Ni
(16) I	Pt/MgAl <sub>2</sub> O <sub>4</sub> [author]				.12 .12	.65	25	321*	*Area under avg. stress/strain curve
(17) I†	Al/MgAl <sub>2</sub> O <sub>4</sub> [78]	1.4/3.6	.27 .26	275/254	.10 .10	.75	41	547	†Liq. ph. sintered 1650C, Al continuous?

Table II (Continued)

(ID) Type	M/C [ref.]	$K_{IC} / K_{IC}$ (MPa $\sqrt{m}$ )	$v_m / v_c$	$E_m / E_c$ (GPa)	$V_{t, bulk} / V_{t, eff}$	$a_o$ ( $\mu m$ )	$\Delta G$ (J/m <sup>2</sup> )	$\Delta G / V_{t, eff} a_o = U$ (MJ/m <sup>3</sup> )	Comments
(18) II	Co/TiC [77]	5/15	.2 .22	450/402	.20 1	.81	479	591	Lig. phase sintered cemented carbide
(19) II	Ru/TiC [77]	5/13	.2 .23	450/440	.60 1	1.13	310	274	"
(20) II†	Al/Al <sub>2</sub> O <sub>3</sub> [40]				.20 1	2	-235**	118	†Lanxide™ process **calc. by avg. $u'/R$
(21) I	Pt/MgAl <sub>2</sub> O <sub>4</sub> [author]				.12 .12	3	13.9	36.3*	*Area under avg. stress/strain curve
(22) I	Mo/WC-Co [46]	12.9/14.1	.23 .24	608/585	.13 .13	5	61	94	Particles/cem.carb.matri x, 1350C
(23) I	Pt/MgAl <sub>2</sub> O <sub>4</sub> [author]				.12 .12	6	16.5	22.9*	*Area under avg. stress/strain curve
(24) I	Nb/TiAl [11]*	12.5/22.5 □	.30 .31	200/175	.20 1	12.5	1904	152	□Nb pancakes, avg for 2 orientations
(25) I	Pb/glass [45]	0.4/0.95	.2 .44	70/59	.20 .20	15	10.1	3.4	Pb particles in glass matrix
(26) I	Mo/WC-Co [46]	12.9/19.4	.23 .24	608/550	.13 .13	55	386	54	Particles/cem.carb. matrix, 1350C

Table II (Continued)

(ID) Type	M/C [ref.]	$K_{IC} / K_{IC}$ (MPa√m)	$v_m / v_c$	$E_m / E_c$ (GPa)	$V_{f,bulk} / V_{f,off}$	$a_o$ (μm)	$\Delta G$ (J/m <sup>2</sup> )	$\Delta G / V_{f,off} a_o = U$ (MJ/m <sup>3</sup> )	Comments
(27) I	Nb/MoSi <sub>2</sub> [41]★	5/23			.20 .20	90	207#	11.5	#Reported, 1350C HIP, interface rxn
(28) I	Nb/WC-Co [46]	12.9/21.6	.23 .26	608/470	.17 .17	100	666	49.2	Particles/cm carb. matrix, 1350C
(29) III	W-3Re/ TiTaAl [79]★	4.5/55	.23 .23	190/215	.16 .16	38 <sup>a</sup> 187 <sup>b</sup>	13225	442	<sup>a</sup> radius of fibers <sup>b</sup> debond length/2
(30) III	Nb/TiAl [49]★					75 <sup>a</sup> 188 <sup>b</sup>	38664	-515 from s.-s. curve	<sup>a</sup> plate 1/2 thickness <sup>b</sup> debond length/2
(31) IV	Nb/MoSi <sub>2</sub> [80]★				.20 .20	125 <sup>a</sup> 375 <sup>b</sup>	20910†	279	†Chevron notch test ⊥ to Nb foils
(32) III	Nb/TiAl [48]★					1000 <sup>a</sup> 1000 <sup>b</sup>	337289	-338 from s.-s. curve	<sup>a</sup> radius of wire (1) <sup>b</sup> debond length/2
(33) III	Pb/glass [10]					1100 <sup>a</sup> 1760 <sup>b</sup>	22328	-20.3 from s.-s. curve	<sup>a</sup> radius of wire (1) <sup>b</sup> debond length/2
(34) III	Pb/glass [6]					125 <sup>a</sup> 500 <sup>b</sup>	6373	-25.1 from s.-s. curve	<sup>a</sup> plate 1/2 thickness <sup>b</sup> debond length/2
(35) III	Nb/MoSi <sub>2</sub> [41]★					65 <sup>a</sup> 390 <sup>b</sup>	85995	-1323 from s.-s. curve	<sup>a</sup> plate 1/2 thickness <sup>b</sup> debond length/2

fibers are present, the effective volume fraction is the bulk volume fraction of fibers.

Type IV laminate composites are represented in Table II by a composite of alternating Nb foils and MoSi<sub>2</sub> (# 31). As the composite was tested in a manner such that the crack propagated perpendicular to the Nb foils, this sample is more similar to a Type III multi-fiber composite. For this particular case, the effective volume fraction of ductile material in the crack path is the bulk volume fraction of Nb in the composite. The appropriate scale parameter for this exceptional case is half of the total debond length for the Nb foils. For multi-layered composites tested in a more conventional manner, however, the appropriate scale parameter would be the half-thickness of the ductile layer and the effective volume fraction would be 1, as the crack path is typically confined to the metal/ceramic interface.

The composite systems of Table II that exhibit interfacial reaction layers are marked by a \* in the 'M/C' column. Brittle reaction layers have been observed in the Nb/TiAl and Nb/MoSi<sub>2</sub> systems, where significant debonding occurs within the brittle layers. Note also that the W-3Re fibers of Composite 29 are coated with a layer of Al<sub>2</sub>O<sub>3</sub> to prevent interdiffusion, and that debonding occurs at the W-3Re/Al<sub>2</sub>O<sub>3</sub> interface.

## 2.2 TRENDS IN TOUGHENING ON THE MICROMETER SCALE

The trends in composite toughening due to ductile bridging are shown graphically in Figure 14, Figure 15, and Figure 16, where  $\Delta G_c/V_{f, effective}$  is plotted against the scale parameter,  $a_0$ , for the broad range of metal/ceramic composites in Table II. The increase in toughness per unit volume at the large end of the scale, where  $a_0 > 50 \mu m$ , is shown in Figure 12. Composites 27, 29, 30, 31, and 35 all have brittle reaction layers at the interface which facilitate debonding. These composites seem to form one grouping, with  $\Delta G$  increasing linearly with the scale parameter  $a_0$ . Toughening is lower in the Pb/glass composites, #33 and #34.

Since constraint has profound effects on the deformation properties of ductile bridging phases, unusual trends in toughening might be expected at the 0-10  $\mu m$  end of the size range. Toughening behavior in the Co cemented carbides and in the remaining composite systems of Table II is shown in Figure 15 as a function of ligament radius. Superior mechanical properties are exhibited by the cemented carbides due to the extremely strong bond between Co and WC, and due to careful optimization of the composite microstructure.

The toughening behavior in composite systems other than Co-WC is highlighted in Figure 16. As a point of comparison, the uniaxial yield strengths for the metal phases are noted in parentheses. The bulk yield strength for the Ni composites was estimated from the measured hardness of similarly processed Ni spheres. The Ni phase was found to contain large amounts of oxygen which raised the bulk yield strength above that for pure bulk Ni. The uniaxial yield strength noted for Al was determined by measuring yield in Al that was processed similarly to Composite 17. Bulk yield strength for the Al-Cu alloy was approximated from TEM measurements of the precipitate spacing noted in-situ. The values noted for Ru, Pt, Co and Mo are handbook values for the uniaxial proof stress of the pure metals in the annealed condition. With the exception of the Mo/WC-Co composite (#22) the toughening in these micron-scale composites appears to exhibit an increase, and subsequent decrease as the ductile ligament radius grows beyond approximately 1  $\mu m$ . This trend could be influenced by

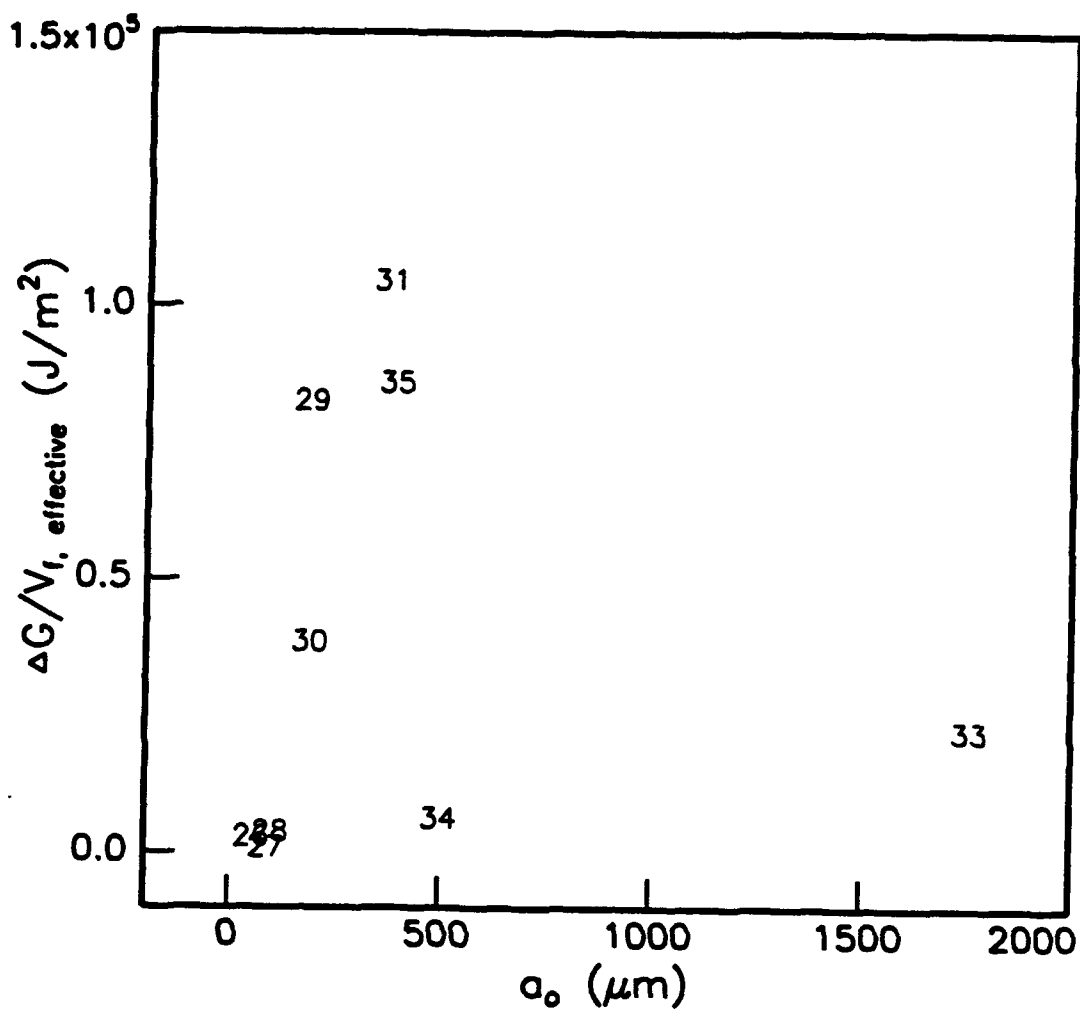


**Figure 14** Toughening per unit volume as a function of the scale parameter,  $a_o$ , for the M/C composites found in Table II, having  $a_o > 50 \mu\text{m}$ .



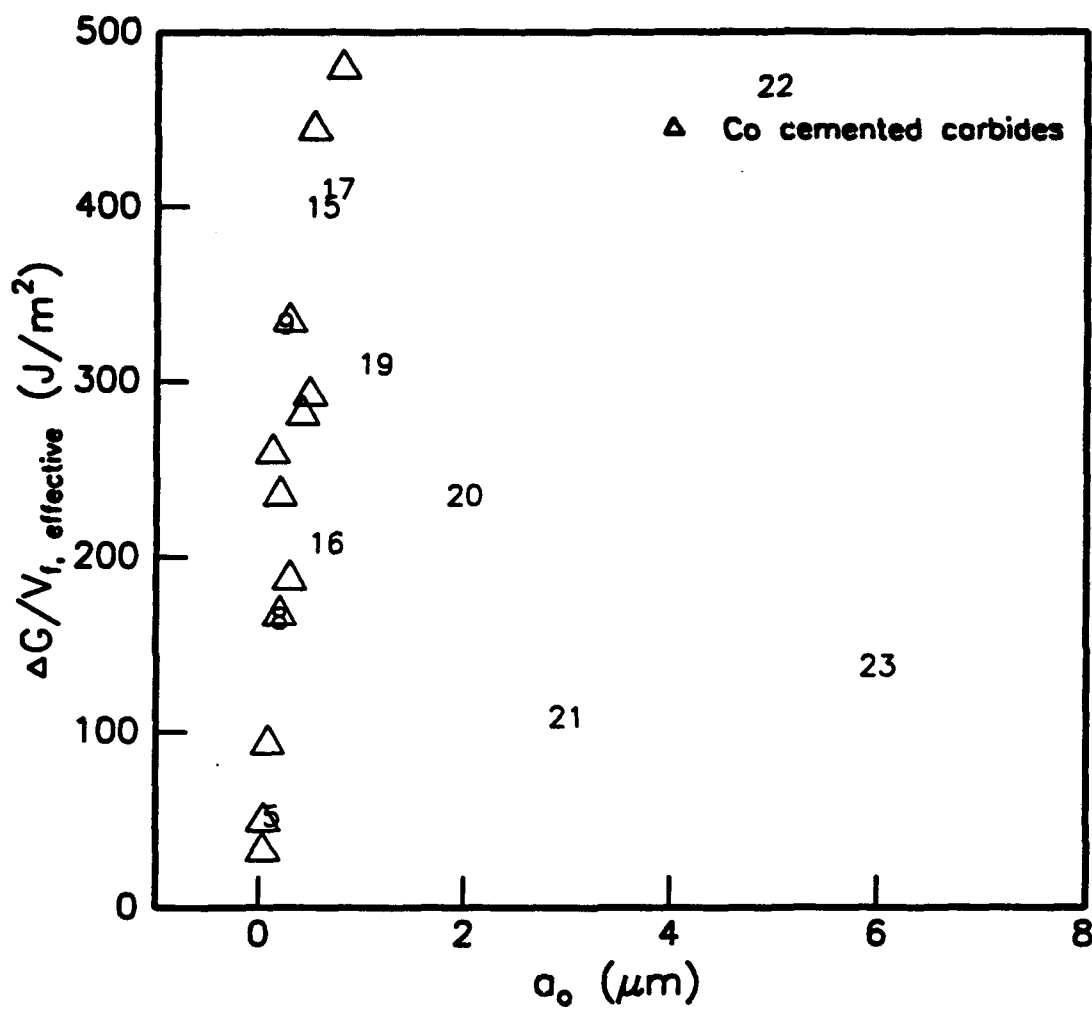


**Figure 15** Toughening per unit volume as a function of the scale parameter,  $a_0$ , for the M/C composites found in Table II, having  $a_0 < 10 \mu\text{m}$ .

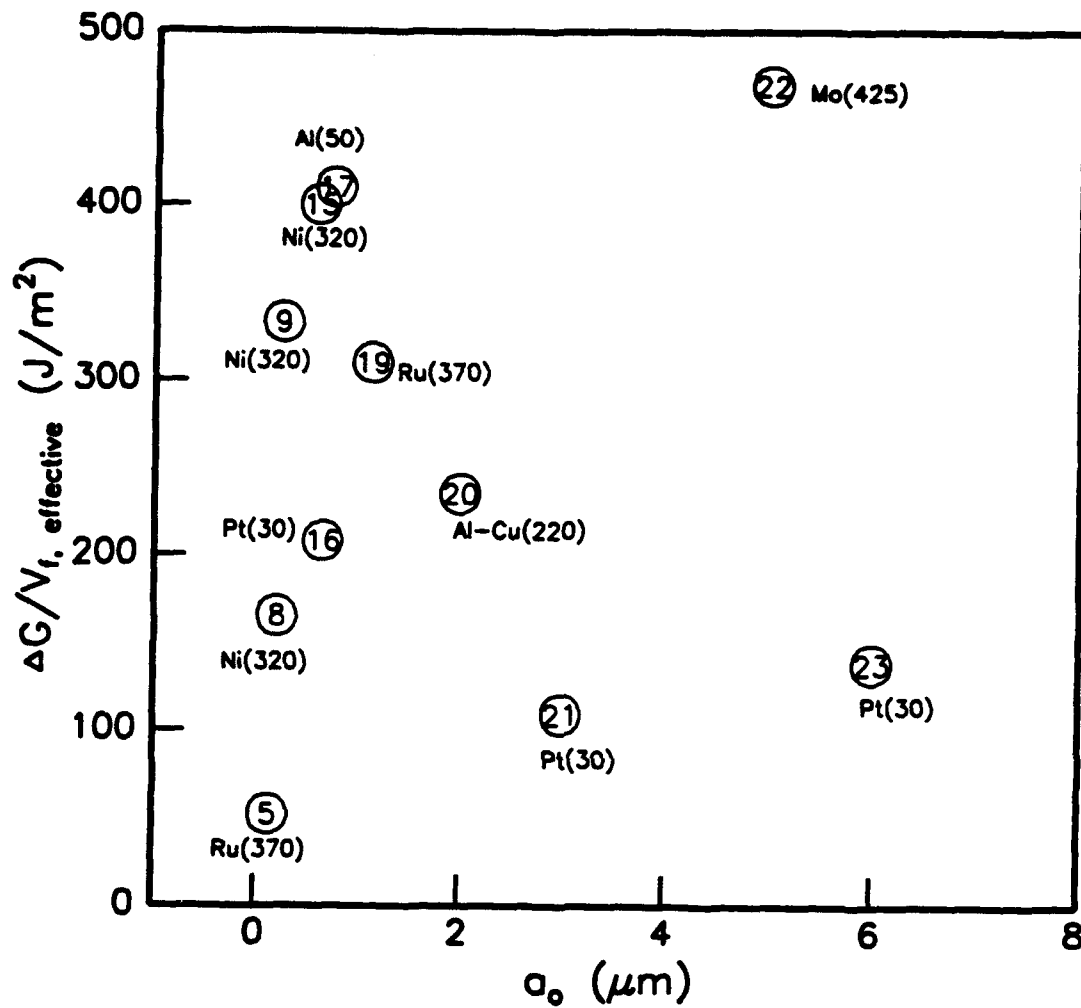


**Figure 16** Toughening as a function of the scale parameter for the non-Co/WC composites found in Table II, having  $a_0 < 10 \mu\text{m}$ . (xxx) denotes the uniaxial yield strength of the metal in MPa.

variations in the base strength of the ductile phase; however, if this were the sole reason, the point for Composite 16 should lie far below that for Composite 8. An explanation for this behavior perhaps lies instead in the influence that a changing level of constraint has upon the deformation behavior of the metal phase.

When small-scale metals are strongly bonded to a rigid matrix, the constraint raises the effective strength of the metal far above the uniaxial stress state value. As was measured in the current study of Pt particles in spinel, the stress in the particles can be 18 times greater than the bulk yield strength. This maximum stress decreases as the particle size becomes larger since constraint accordingly has less influence on the deformation behavior of the metal. As observed in the case of platinum, the larger particle size caused debonding, which also led to loss of constraint. In both cases, a corresponding decrease in the work of plastic deformation should then also occur. As derived earlier, the expression  $\Delta G/V_l a_0$  is equivalent to the area under the stress-strain curve for the average bridging ligament, and thus represents the work done,  $U$ , to plastically deform the ligament to bridging failure.  $U$  is plotted as a function of ligament size for the various composites in Figure 17 and is shown to be an inverse function of size for ductile radii less than approximately 10  $\mu\text{m}$ .

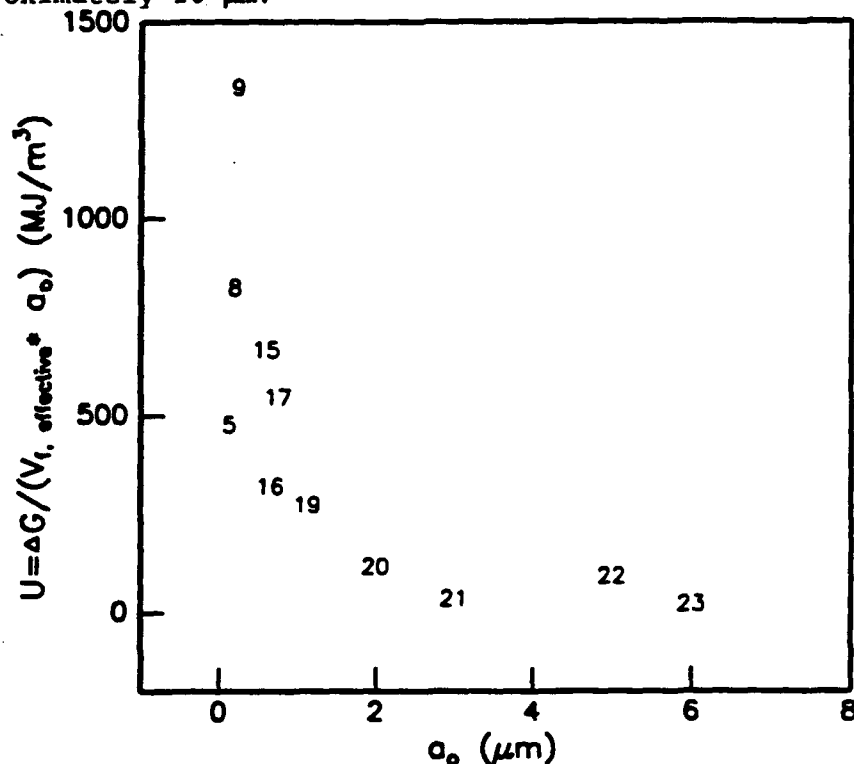


**Figure 17** Work of plastic deformation ( $U$ ) as a function of ductile ligament radius ( $a_0$ ) for the micron-scale composites of Table II.

### 2.3 "MICRO" VS. "MACRO" COMPOSITE BEHAVIOR

This study has demonstrated that the principles of "macro-composite"

behavior do not necessarily apply in the case of "micro-scale" composites. Moderate amounts of debonding are required to accomodate ductility and achieve significant toughening in large scale, fibrous composites, as was shown in the composite cylinder tests of Figure 19.

Debonding has the opposite effect on the work of deformation in micron-scale composites, as shown in the present study of Pt particles in spinel. While large-scale composites are tolerant to localized debonding, this study has shown how localized debonding in micron-scale composites can lead to catastrophic bridging failure. Finally, an analysis of behavior for many different micro-composite systems has shown, in opposition to large-scale composite behavior, that the plastic work of deformation on the micron scale is greatest when constraint is a maximum and bonding is the strongest. [18] [19] [20] [21] [22]

### **3. Single Crystal Based Microstructure Design of Metal Matrix Composites for High Temperature Applications.**

#### **3.1 ABSTRACT**

A microstructure design constructed from fibrous ceramic crystals embedded in a continuous metal matrix with the following features is proposed: ceramic crystals have an aspect ratio greater than 30, the diameter of the ceramic crystals is approximately 5 $\mu$ m, the metal volume fraction is the range 8-30%, the channel width of the metal layers is less than 1 $\mu$ m, and the metal-ceramic interface is coherent. Such a microstructure is likely to have good creep resistance, cavitation resistance and thermal shock resistance.

---

<sup>18</sup>Fracture toughness as an aid to alloy development., T. McLaren and J.B. Lambert, Science of Hard Metals, Ed. R.K. Viswanadham, D.J. Rowcliffe, and J. Gurland, p. 694, (1981)

<sup>19</sup>Indentation testing of a broad range of cemented carbides., R. Warren and H. Matzke, *ibid.*, p. 575

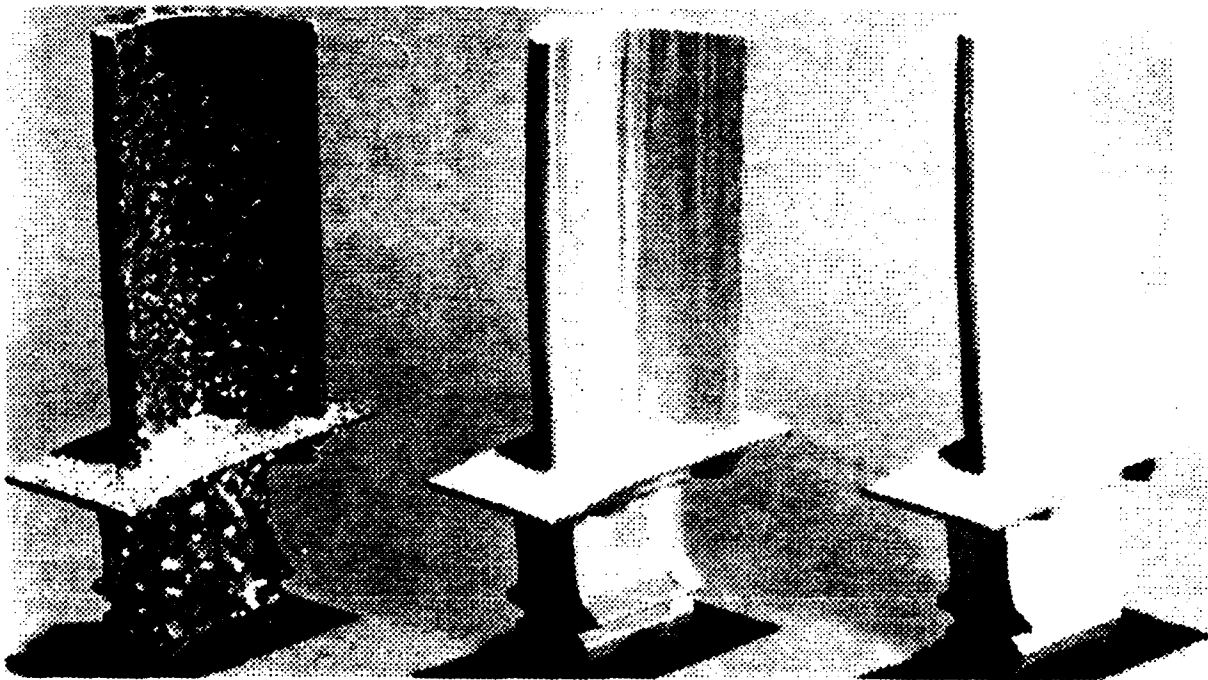
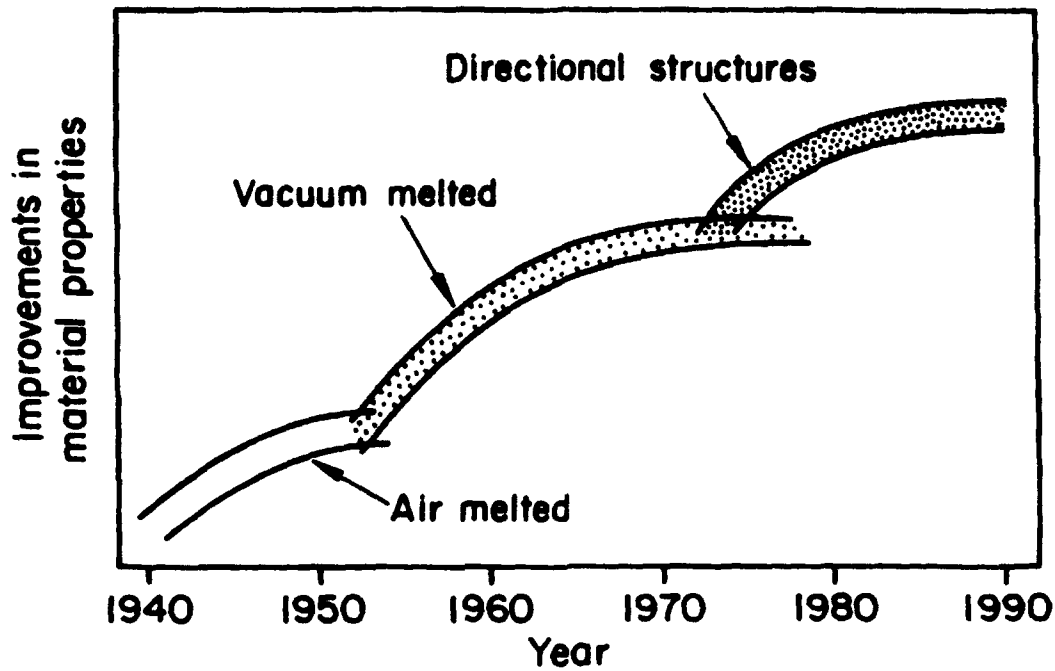
<sup>20</sup>T. Gustafson and P.C. Panda, Cornell Univ., unpublished data

<sup>21</sup>On the toughening of intermetallics with ductile fibers: Role of interfaces., H.E. Dève and M.J. Maloney, *Acta Met.*, 39 [10], 2275-2284, (1991)

<sup>22</sup>Role of matrix/reinforcement interfaces in the fracture toughness of brittle materials toughened by ductile reinforcements., L. Xiao and R. Abbaschian, *Met. Trans. A*, 23A, 2863-2872, (Oct, 1992)

## Superalloys

### 3.2 INTRODUCTION



**Conventional casting      Columnar grain      Single crystal**

**Figure 18:** The three eras in the evolution of the superalloys.  
Directional solidification led first to the columnar grain structure and eventually to single crystal turbine blade.

3.2.1 *The Design of Superalloys*: Today's superalloys serve in structural applications at a higher fraction of their melting temperature than any other material. The highest temperature applications are found in turbine blades, which are in the form of single crystals, in jet engines for passenger aircraft[23].

There have been two major developments in the evolution of present day superalloys (Fig.18) [24],[25]. In the early fifties vacuum melting was introduced to lower the oxygen content resulting in greater resistance to intergranular cavitation. Then, in the mid-seventies, directional solidification was adopted to make high aspect ratio grain structures with boundaries aligned parallel to the loading axis. Different types of directional microstructures were explored, including directionally solidified eutectics. However, best properties were achieved where the entire component consisted of a single crystal[26].

In the single crystal approach the emphasis in basic research moved from the study of intergranular cavitation to the understanding of creep by dislocation mechanisms. Today, the superalloy single crystals consist of a solid solution strengthened nickel  $\gamma$  matrix reinforced by intermetallic  $\gamma'$ . The volume fraction of  $\gamma'$  can be greater than 70% and it is produced by precipitation.

The use of elongated grain structure is another way of obtaining single crystal like properties at high temperatures. This approach has been used effectively in the design of ODS alloys[27],[28], and also in the design of the tungsten filaments for incandescent lamps[29].

---

<sup>23</sup> Sims C.T., Stoloff N.S., and Hagel J., eds., Superalloys II, (John Wiley and Sons, New York, 1987).

<sup>24</sup> G. S. Hoppin III and W. P. Danesi, "Future of Superalloys", *ibid.* Ref. 1, pp. 549-561.

<sup>25</sup> M. Gell and D. N. Duhl, "The Development of Single Crystal Superalloy Turbine Blades", in Processing and Properties of Advanced High Temperature Alloys, (eds) S. Allen, R. M. Pelloux and R. Widmer, (American Society for Metals, Metals Park, OH 1986), 97-131.

<sup>26</sup> E. W. Ross and C. T. Sims, "Nickel-Base Alloys", *ibid.* Ref.1, 97-131.

<sup>27</sup> B. A. Wilcox and A. H. Clauer, "High Temperature Creep of Ni-TiO<sub>2</sub> Alloys", in Oxide Dispersion Strengthening, (eds) G. S. Ansell, T. D. Cooper and F. V. Lenel, (Gordon and Breach, New York, 1968), 323-356.

<sup>28</sup> E. Arzt and R. F. Singer, "The Effect of Grain Shape on Stress Rupture of the Oxide Dispersion Strengthened Superalloy MA6000", in Superalloys 1984, (eds) M. Gell et al., (The Metallurgical Society, 420 Commonwealth Drive, Warrendale, PA 1984), 361-371.

<sup>29</sup> R. Raj and G. W. King, "Life Prediction of Tungsten Filaments in Incandescent Lamps", Metall. Trans. A, 9A (1978), 941-946.

**3.2.2 The Design of Ceramic Reinforced Metal Matrix Composites:** The highest possible service temperature of single crystal nickel base superalloys is limited by dislocation creep. The coarsening of the  $\gamma'$  precipitates and deformation of the intermetallic phase become significant above 1000°C. Thus higher service temperatures should be possible if the intermetallic  $\gamma'$  is replaced by an ceramic oxide.

The purpose of this paper is to consider the design guidelines for the microstructural features of the above ceramic reinforced metal-matrix composite. The criteria that must be considered in this design process are: (a) creep resistance, (b) cavitation fracture resistance of the metal-metal and the metal-ceramic interface, (c) resistance to thermal shock, and (d) resistance to environmental degradation. In the following sections we consider the first three criteria. The first of these leads to the concept of a single crystal like structure consisting of elongated ceramic grains embedded in an interconnected metal matrix. The second and the third criteria lead to guidelines for the scale of the microstructure, the volume fraction of the interconnected metal phase, and the atomic structure and bonding of the metal/ceramic interface.

The choice of the metallic phase is limited by environmental stability. While refractory metals with their very high melting points and with thermal expansion coefficients close to those of oxides are interesting (the melting points are W-3410°C, Mo-2610°C, Ta-2996°C, and Nb-2468°C, and the thermal expansion coefficients in units of  $10^{-6}$  are W-4.6, Mo-5.8, Ta-6.7 and Nb-8.3)[30], they suffer from poor oxidation resistance, especially Ta, Mo and W which form volatile oxides[31]. In this context, it is interesting to note that the latest research in superalloys is concentrated in the development of oxide coatings that can serve as a barrier to thermal conduction, allowing higher inlet gas temperatures[32]. These coatings are often required to have the same properties that will be needed to protect the metal in the metal matrix composites from oxidation at very high temperatures.

---

<sup>30</sup> R. G. Frank, "Recent Advances in Refractory Alloys", in Refractory Metal Alloys: Metallurgy and Technology, (eds) I. Machlin, R. T. Begley and E. T. Weisert, (Plenum, New York, 1968), 325-372.

<sup>31</sup> However, niobium is a promising candidate. Its density is nearly the same as nickel, it does not suffer from a ductile to brittle transition, forms a solid oxide and has the potential of being hardened by precipitation of carbides or by solid solution strengthening. The thermal expansion coefficient of Nb matches that of alumina. It is also chemically compatible with alumina and probably with other oxides as well.

<sup>32</sup> J. H. Wood and E. H. Goldman, "Protective Coatings", *ibid.*, Ref.1, 359-383.

### 3.3 SINGLE CRYSTAL DESIGN FOR CREEP RESISTANCE

Two mechanisms, dislocation creep[33] and diffusional creep[34],[35], contribute to the deformation of structural materials at service temperatures. Dislocation creep is grain size independent and, therefore, important in "single crystal" designs. Diffusional creep is most easily suppressed by increasing the grain size. Both mechanisms are diffusion controlled; therefore, the use of dopants that bind to vacancies help to lower the rate of creep.

A study of the deformation mechanism maps of pure refractory metals with an equiaxed grain structure, for example niobium[36], shows that the creep rates by the dislocation mechanism are too fast for high temperature structural applications (in pure Nb the dislocation creep rate is nearly  $0.1 \text{ s}^{-1}$  at  $1650^\circ\text{C}$  for an applied stress of only 10 MPa), and that the diffusional creep rates can be reduced to an acceptable level (of approximately  $10^{-8} \text{ s}^{-1}$ ) only if the grain size is larger than  $100\mu\text{m}$ . An equiaxed, two phase microstructure consisting of niobium and an oxide (such as alumina), however, is not likely to improve the creep resistance very significantly. Furthermore, crystal slip in the metal grains that are  $100\mu\text{m}$  will produce large stress concentrations at the metal ceramic interface with a high probability of inducing interface fracture.

The "single crystal" microstructure that we propose for the metal matrix composite is similar to the design of the single crystal superalloy, consisting of elongated grains of a ceramic embedded in a metallic matrix. The two critical issues in the performance of this design are as follows:

- (a) **The structure of the metal-ceramic interface:** The best properties will be obtained if the metal-ceramic interface is coherent, which would impart resistance to dislocation creep, to creep cavitation and to cleavage fracture at the metal/ceramic interface.
- (b) **Thermal shock properties of the metal/ceramic composite:** A difference in the thermal expansion coefficients of the metal and the ceramic, and the anisotropy in the thermal expansion coefficient of the ceramic, can induce cleavage damage at the m/c interface. Microstructure designs that reduce the probability of this damage must be considered.

In the following sections the above issues are discussed one by one. The features of the microstructure that is proposed are shown by the

---

<sup>33</sup> A. K. Mukherjee, J. E. Bird and J. E. Dorn, "Experimental Correlations for High Temperature Creep", Trans. Amer. Soc. Met., 62 (1), (1969), 155-179.

<sup>34</sup> C. Herring, "Diffusional Viscosity of Polycrystalline Solids", J. Appl. Phys., 21 (1950), 437-445.

<sup>35</sup> R. L. Coble, "A Model for Boundary Diffusion Controlled Creep in Ceramic Materials", J. Appl. Phys., 34 (6) (1963), 1679-84.

<sup>36</sup> H. J. Frost, Deformation Mechanism Maps, Ph.D. Thesis, Harvard University, Cambridge MA, January 1974.



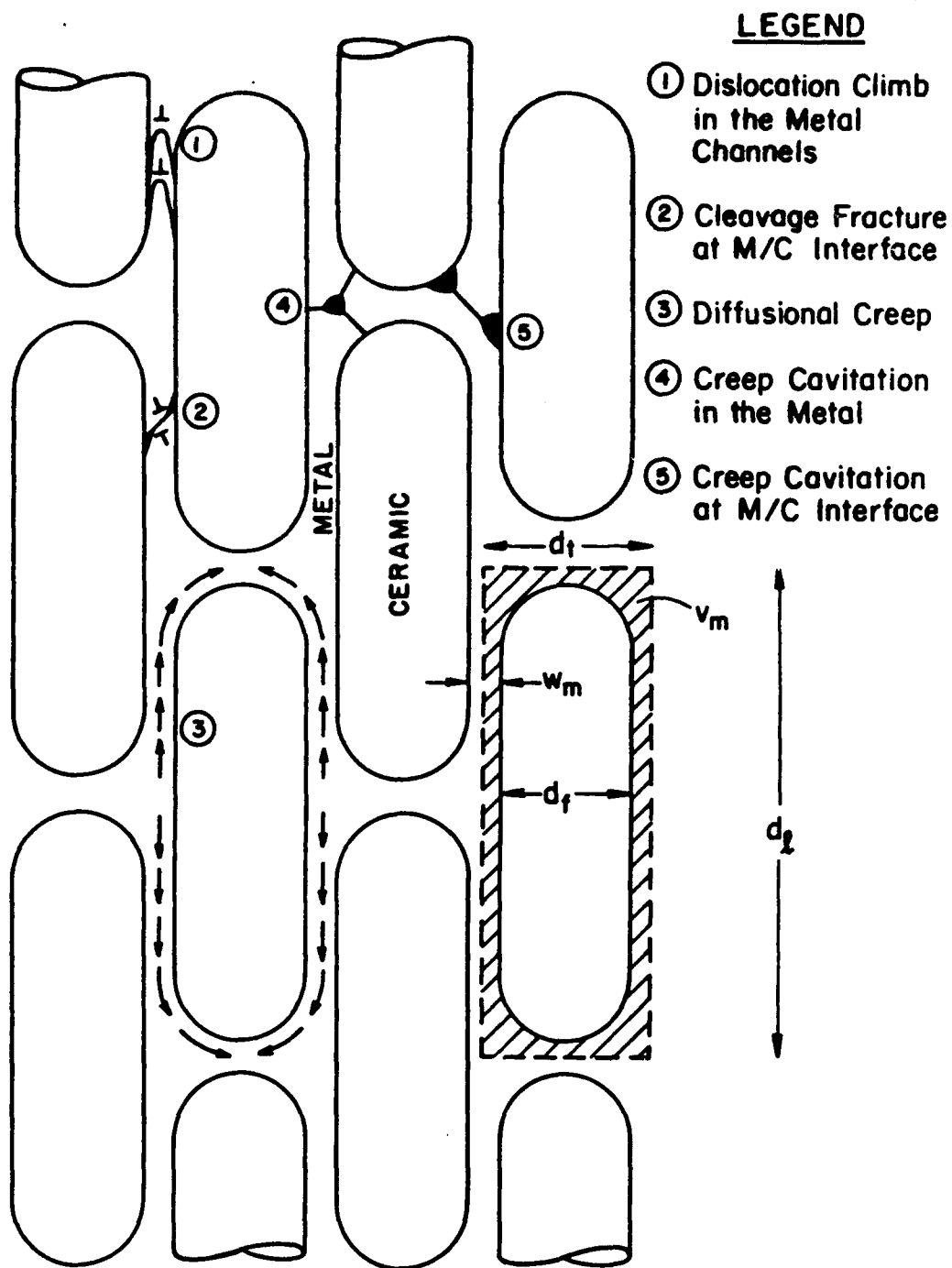


**Figure 19:** The geometrical parameters for the metal/ceramic composite. Item numbers 1 through 5 illustrate the possible deformation and fracture mechanisms in the composite.

schematic in Fig. 19. The ceramic grains are assumed to have a fibrous structure. The "unit cell" of the microstructure is defined by the transverse dimension  $d_t$ , the fiber diameter  $d_f$ , and the longitudinal dimension  $d_l$ . The other important microstructural parameters are  $v_m$ , the volume fraction of the metal phase, and  $w_m$ , the width of the metal channels confined in between the adjacent ceramic grains. Simple geometric analysis leads to the following relationship between these parameters:

$$\frac{w_m}{d_t} = \frac{1}{4} \left( v_m - \frac{1}{3A_r} \right) \quad (11)$$

Where the aspect ratio is defined as:

$$A_r = \frac{d_l}{d_t} \quad (12)$$

Note that the right hand side in Eq. (11) must be greater than zero to obtain a continuous metal phase. The plot in Fig. 20 shows that the minimum volume required to obtain interconnectivity decreases with increasing aspect ratio. The width of metal film,  $w_m$ , varies with  $A_r$ , although it approaches a plateau for a fixed volume fraction as  $A_r$  becomes large. This limit, obtained from Eq. (11), is as following:

$$\lim_{A_r \rightarrow \infty} \left( \frac{w_m}{d_t} \right) = \frac{v_m}{4} \quad (13)$$

Equation (13) provides a useful guideline for microstructure design. For example suppose that the width of the metal films must be less than  $1\mu\text{m}$  (in order to achieve a sub-critical length of dislocation pile up), and that the diameter of the ceramic fiber is  $50\mu\text{m}$ , then the volume fraction of the metal must be less than 8%. However, if the fiber diameter can be reduced to  $10\mu\text{m}$  then the volume fraction of the metal may be as high as 36% (note that  $d_t = d_f + w_m$ ).

The properties of the conceptual microstructure sketched in Fig. 19 are discussed in the following sections. It is important to keep in mind that these properties depend critically on the atomic structure of the interface. The possible ways of envisioning this coupling between the atomic structure of the interface and the macroscopic behavior is discussed in the last section.

**3.3.1 Diffusional Creep:** Diffusional creep requires interfaces where atoms can be plated or removed[37] to produce a change in shape. If the entire composite structure is made of one single crystal then diffusional

---

<sup>37</sup> R. W. Balluffi, "High Angle Grain Boundaries as Sources and Sinks for Point Defects", Grain Boundary Structure and Kinetics, (American Society for Metals, Metals park OH, 1980), 297-329.

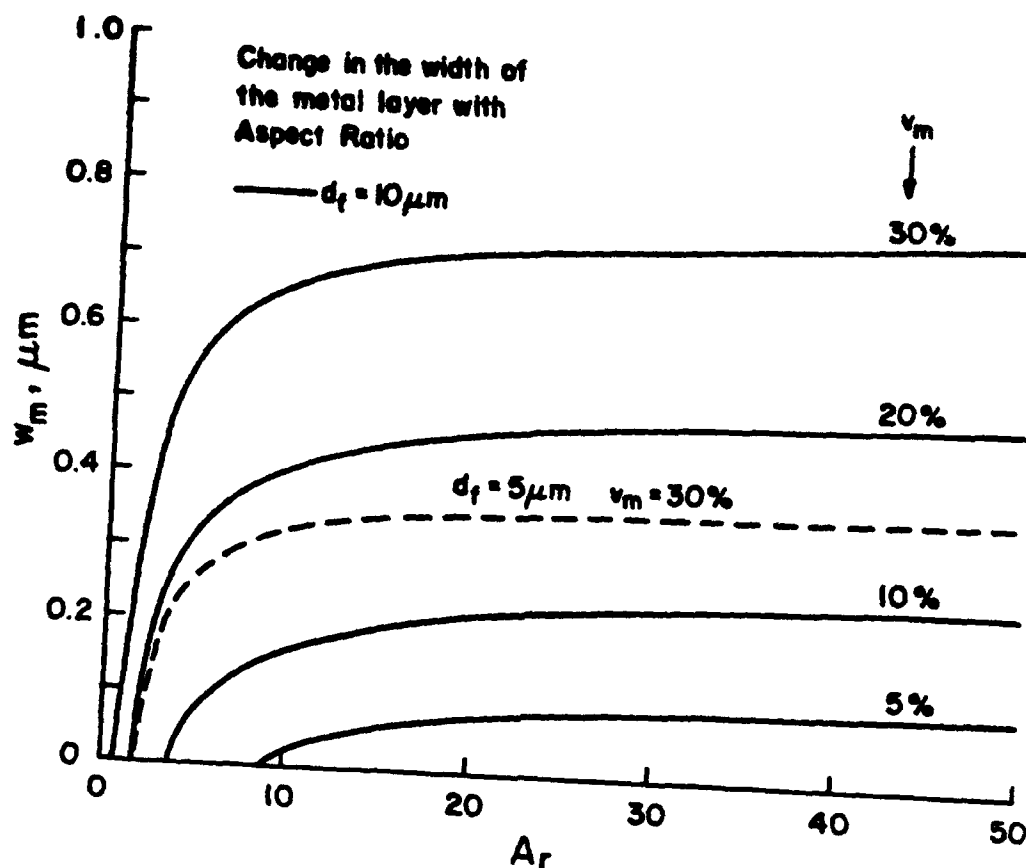


Figure 20: The relationship between the width of the metal layer and the aspect ratio of the ceramic crystals, for different volume fractions of the metal. Two cases of fiber diameters have been considered.

creep will be suppressed. The metal/ceramic interface cannot by itself serve both as a source and a sink of atoms if the inclusions are rigid[38]. However, let us consider the more likely situation that the metal does contain interfaces so that diffusion by the path illustrated in Fig. 19 leads to creep. This mechanism can be analyzed approximately as follows. We assume that a tensile stress,  $\sigma$ , is applied along the longitudinal direction and that this stress drives diffusion from the longitudinal plane to the transverse plane, through the cross section of the metal layer of thickness  $w_m$  surrounding the rigid ceramic grains. Lattice diffusion through the metal is likely to be the dominant diffusion mechanism, and assuming the average diffusion distance to be  $d_f/4$  the atom

<sup>38</sup>The transport of atoms around the inclusion from the longitudinal to the transverse interface can lead to transient creep that would accommodate the elastic stresses generated by the difference in the moduli of the metal and the ceramic, but it cannot lead to steady state creep. The total magnitude of the transient creep will be of the same order as the elastic strain.

flux will be given by:  $J_V = (D_V/\Omega kT) (4\sigma\Omega/d_1)$ , where  $D_V$  is the lattice self diffusion coefficient of the metal,  $\Omega$  is the atomic volume, and  $\sigma\Omega$  is the maximum chemical potential difference between the atoms at the longitudinal and transverse interfaces. The flux is translated into strain rate using the equation that

$\dot{\epsilon} = (J \cdot \pi d_t w_m \Omega / 2) (4/\pi d_t^2) (1/d_1)$ , where the first term is the volume being plated on the transverse interface, the second term converts that into displacement rate and the third term converts it into strain rate. Substituting from Eq. (12) and (13) then leads to the following result:

$$\dot{\epsilon} = 2 \frac{\sigma \Omega}{kT} \frac{v_m D_V}{A_r d_f^2} \quad (14)$$

According to Eq. (14) the strain rate is inversely proportional to the aspect ratio of the ceramic fibers and inversely proportional to the diameter of the ceramic fibers (assuming that  $d_t = d_f$ ). The volume fraction of the metal phase has a minor influence on the strain rate: they are linearly proportional to each other.  $T/T_M$

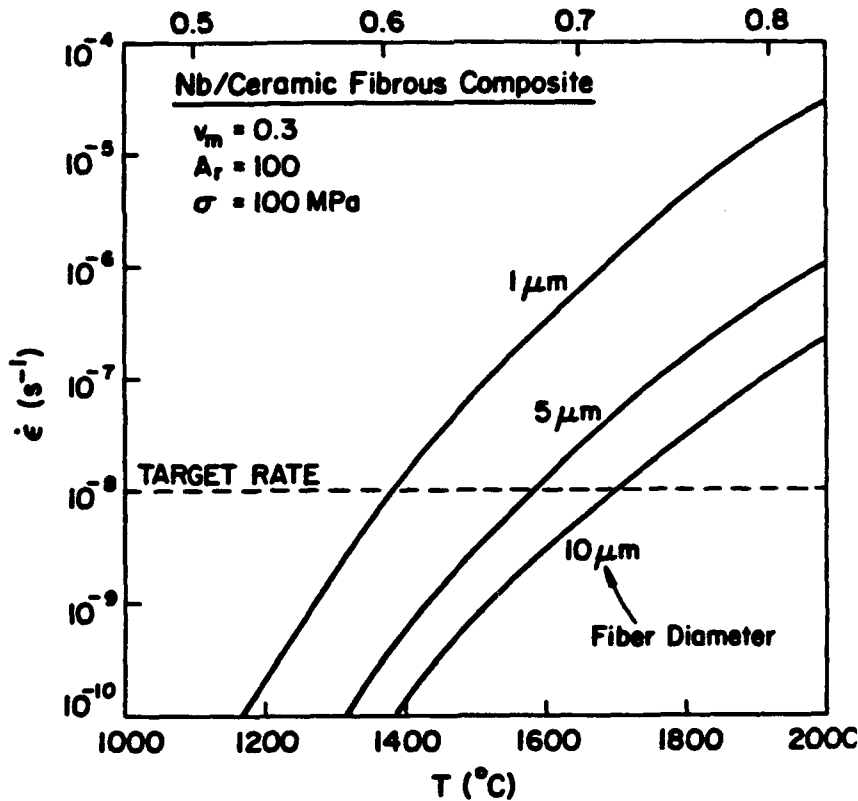


**Figure 21:** The predicted diffusional creep rates of a niobium/alumina composite as a function of temperature.

A plot of Eq. (14) assuming that the metal is niobium (and the ceramic is a non-deforming constituent) is given in Fig. 21. The material

constants for Nb were assumed to be as follows:  $\Omega = 1.8 \times 10^{-29} \text{ m}^3$ , and  $D_v = 1.1 \times 10^{-4} \exp(-402 \text{ kJ mol}^{-1}/RT) \text{ m}^2 \text{ s}^{-1}$ . The curves show that strain rate that can be expected at different temperatures assuming that the applied stress is 100 MPa, the aspect ratio of the ceramic fibers is 100, and the volume fraction of the metal is 30%. The results for three values of the fiber diameter 1, 5 and 10  $\mu\text{m}$  are shown. Note that fiber diameters that are greater than 5  $\mu\text{m}$  yield a strain rate of less than  $10^{-8} \text{ s}^{-1}$  at 1600°C.

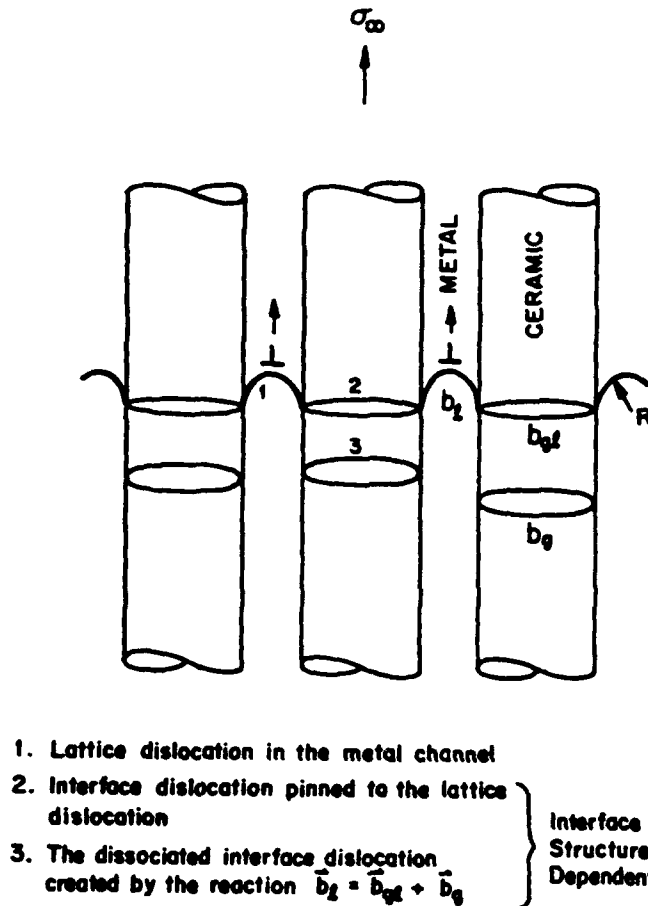


**Figure 22:** It is postulated that the lattice dislocation dissociates into two interface dislocations, one of whom,  $b_{gl}$ , is pinned to the lattice dislocation.

**3.3.2 Dislocation Creep:** Single crystal nickel base  $\gamma/\gamma'$  superalloys deform by dislocation creep. The mobility of dislocations has been studied in the

literature, most recently by Pollock and Argon[39] who have investigated the mechanism by which the dislocations move through the  $\gamma$  phase channels formed in between the cuboidal  $\gamma'$  precipitates. The width of these channels is typically  $0.1\mu\text{m}$ , which is less than the spacing between dislocations; thus, when forced to move the  $\gamma$  dislocations become pinned by walls of  $\gamma/\gamma'$  interfaces. The mechanism of pinning is likely to be related to the structure of the interface. The lattice mismatch between the  $\gamma$  and  $\gamma'$  has an influence on the creep behavior[40]. In low  $\gamma'$  volume fraction alloys the zero mismatch appears to give the lowest creep rate but in high volume fraction alloys a non-zero value of the mismatch gives the optimum creep performance[41],[42]. The first result may be rationalized on the basis of the lowest rate of coarsening of  $\gamma'$  precipitates, but the second result suggests a more complex role for the interface structure and bonding on the mobility of dislocations.

The lattice dislocation and the interface dislocation are two different entities with their own Burgers vector, which we call  $b_l$  and  $b_{gl}$ , respectively. They will be equal if the lattice dislocation does not disassociate when it enters the boundary; if it does, then we must invoke a vector equation:  $b_l = b_{gl} + b_g$ , where  $b_g$  is a dislocation that is totally embedded in the interface and its structure is related to the interface structure (for example,  $b_g$  could be a van der Merwe[43] dislocation that accommodates the misfit strain between the two lattices). This disassociation is illustrated by the schematic in Fig. 22.

The lattice and interface dislocations,  $b_l$  and  $b_{gl}$ , must move together. The leading and the lagging dislocation segments will have opposite curvatures in the moving configuration. The case where the interface dislocation has the lower mobility is illustrated in Fig. 23.

We now estimate the driving force for dislocation climb assuming that the interface dislocation is rate controlling. We obtain an expression for the force on the interface dislocation loop represented by ( $b_{gl}$ ,  $\mathcal{E}_{gl}$ ) in Fig. 23. ( $\mathcal{E}_{gl}$  and  $\mathcal{E}_l$  are the line tensions for the interface and the lattice dislocations). The total force on the interface dislocation loop consists of two terms: (i) the force expressed on the loop directly by the applied stress, which is equal to  $\sigma b_{gl} \pi d_l$ , where  $\sigma$  is the applied stress, and (ii) the pulling force exerted by the curved lattice dislocation, which would be equal to  $2\mathcal{E}_l \cos\theta$ . The angle  $\theta$  is related to the curvature in the lattice segment of the dislocation. It can be expressed in terms of the applied stress and the width of the metal channel,  $w_m$ , leading to the following expression for the driving force,  $F$ :

---

<sup>39</sup> T. M. Pollock and A. S. Argon, "Creep Resistance of CMSX-3 Nickel Base Superalloy Single Crystals", Acta Metall. Mater., 40 (1) (1992), 1-30.

<sup>40</sup> I. L. Mirkin and O. D. Sancheev, Met. Sci. Heat Treatment, vol (1,2) (1967), p.10, referenced in "Fundamentals of Strengthening" by N. S. Stoloff, Ref. *ibid* 1, p 61.

<sup>41</sup> C. C. Law and M. J. Blackburn, Metall. Trans. A, 11 (1980), 495.

<sup>42</sup> F. Schubert, Superalloys Source Book, (ASM, Metals Park, OH 1984); referenced by S. Floreen in "Mechanical Behavior", *ibid* Ref. 1, p. 241.

<sup>43</sup> J. H. van der Merwe, Surface Science, 31 (1972), 198.

## HIGH INTERFACE FRICTION

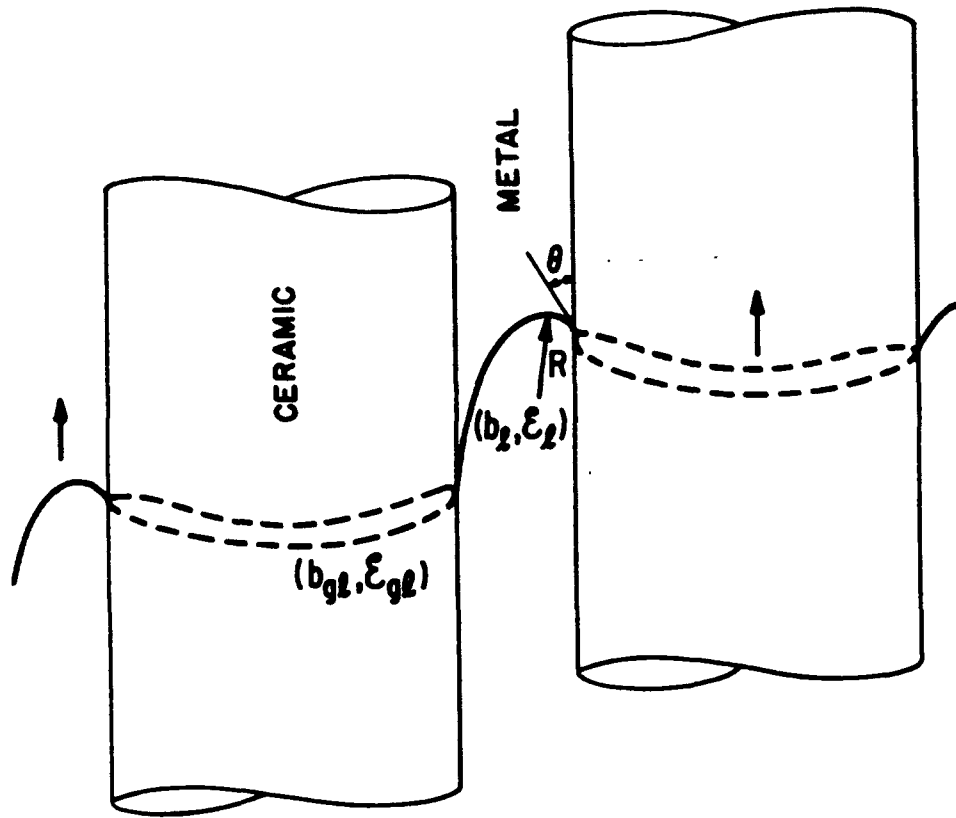


**Figure 23:** The moving configuration of a lattice and an interface dislocation where they are pinned to each other, and where the interface dislocation is assumed to be slower moving.

$$F = \sigma b_{gl} \pi d_f + \sigma b_l w_m \quad (15)$$

Further simplification of the Eq. (15) results by expressing it in terms of the Orowan stress,  $\sigma_{ow} = \mathcal{E}_l / (b_l w_m)$ , by assuming that  $d_f = d_l$  and by substituting from Eq. (13), which gives that:

$$\frac{F}{\mathcal{E}_l} = \frac{2\sigma}{\sigma_{ow}} \left( \frac{4\pi}{v_m} \cdot \frac{b_{gl}}{b_l} + 1 \right) \quad (16)$$

The second term in the above equation represents the pulling force on the loop from the lattice dislocation; this force reaches its maximum value when  $\sigma = \sigma_{ow}$ , and becomes constant if the stress is increased further since the maximum possible force on the loop is reached when  $\theta = 0^\circ$ . The issue is not important since the first term will be generally greater than unity and, therefore, will dominate the force exerted on the interface loop. Thus, it appears as if the rate of creep is controlled not by the bowing

out of the lattice dislocations but by the force exerted by the applied stress directly on the interface dislocations.

The analysis presented above assumes that the interface dislocations climb more slowly than lattice dislocations. The picture of dislocation movement presented in Figs 22 and 23 is consistent with the work of Pollock and Argon. The mobility of interface dislocations would depend greatly on the structure of the interface and the diffusivity of point defects in the interface. In general, if the bonding at the metal/ceramic interface is strong then interface dislocations will have low mobility.

### 3.3 RESISTANCE TO THERMAL SHOCK

Thermal shock, or more precisely, accumulative cyclic damage resulting from a difference in the thermal expansion of the metal and the ceramic will be a critical issue in the design of metal/ceramic composites. The figure of merit for thermal shock resistance in ceramics is given by:

$$\Delta T_c = B \frac{\sigma_f}{\alpha E} \quad (17)$$

where  $\Delta T_c$  is the maximum step change in temperature that can be sustained without fracture damage,  $\sigma_f$  is the tensile fracture strength,  $\alpha$  is the coefficient of linear thermal expansion,  $E$  is the Young's modulus, and  $B$  is a constant, called the Biot number, that depends on heat transfer parameters and sample size. In high volume fraction metal ceramic composites Eq. (17) is likely to provide reasonable guidelines for obtaining threshold values for safe and unsafe temperature excursions. The detailed microstructure design of the metal/ceramic composite, however, must be based on fracture mechanism. The mechanism proposed here is slip induced interface fracture as illustrated in Fig. 19 by mechanism #2. There are three criteria that can be set for this type of microfracture: (i) a stress criterion that asks that the local stress concentration should be large enough to induce fracture, (ii) an elastic strain energy criterion that is equivalent to the Griffith condition, and (iii) a displacement criteria that is linked to the local strain that must be supplied in order to meet the need for physical opening of the cleavage crack. Below we evaluate these criteria to seek a threshold failure condition.

Criterion (iii) has been discussed in a fundamental way by Stroh[44] and applied specifically to slip induced cleavage initiation by Cottrell[45]. It requires a minimum amount of plastic strain. This condition cannot lead to a threshold since plastic strain may accumulate over several thermal cycles. However, a composite that has good ductility will also have better thermal shock resistance.

The local stress and the strain energy criterion depend on the scale and the morphology of the microstructure, represented by  $w_m$  and  $A_f$  in Fig.

---

<sup>44</sup> A. N. Stroh, Advances in Physics, 6 (1957), 418.

<sup>45</sup> A. H. Cottrell, "Theory of Brittle Fracture in Steel and Similar Metals", Trans. AIME, 208 (4) (1958), 192-203.



19. The difference in the thermal expansion coefficient of the metal and the ceramic will give rise to spatially periodic tensile and compressive stresses, on the scale of  $d_c$ . Since fracture can occur only if the stress is tensile, the Griffith fracture condition must reflect the microstructural scale. Analysis[46] of this problem leads to the following threshold condition for failure:

$$d_f \leq \frac{4}{3} \frac{\gamma_{eff} F_s}{F_v E (\Delta T \Delta \alpha)^2}, \quad (18)$$

Here  $\gamma_{eff} = \gamma_m + \gamma_c - \gamma_{mc}$  where the interface energies on the right hand side refer to the free metal surface, free ceramic surface and the metal/ceramic interfaces, respectively.  $\Delta T$  and  $\Delta \alpha$  are the temperature excursion and the difference in coefficients of thermal expansion.  $E$  is the Young's modulus of the metal. The parameter  $F_s$  accounts for the shape of the crack (it may usually be assumed to be equal to  $\pi/2$ ).  $F_v$  is the shape factor for the volume of one "unit cell" (see Fig. 19). For a fixed volume, a spherical shape will have the highest value, a needle shape an intermediate value, and a disc shape the smallest value of  $F_v$ [47]. Thus disc shaped ceramic inclusions are likely to have the best resistance to thermal shock. The magnitude of the right hand side in Eq. (18) is strongly material dependent, and may range from less than 1  $\mu\text{m}$  to 50  $\mu\text{m}$ . Certainly, composites made from thick ceramic fibers ( $d_f > 100 \mu\text{m}$ ) are likely to have poor thermal shock resistance.

The largest stress concentration in the microstructure occur at the metal ceramic interface, where the thermal expansion coefficient is discontinuous. The design of the atomic structure of the interface, with the idea of creating graded interfaces that diffuse this stress concentration can enhance resistance to thermal shock. A first order analysis of the problem leads to the following guidelines: (a) the elastic moduli of the metal should be matched as far as possible to the elastic moduli of the ceramic, and (b) the magnitude of the interfacial shear stress,  $\tau_{mc}$ , at the end corner of the ceramic fiber is related to geometry (assuming that the elastic moduli are matched), by the following equation[23]:

$$\frac{\tau_{mc}}{\Delta \alpha \Delta T E} = \sqrt{\frac{1}{3 \left( v_m - \frac{1}{3 A_r} \right)}} \quad (19)$$

Equation (19) suggests that a large volume fraction of the metal and a

---

<sup>46</sup> R. Raj, "The Design of the Interface Phase for Obtaining Thermal Shock Resistance in Silicon Nitride", International Conference on Thermal Shock, Schloss Ringberg in November 1992, eds., G. Petzow, G. Schneider and M. Hoffmann, to be published by the Kluwer Press, Netherlands (1993).

<sup>47</sup> J. W. Christian, The Theory of Transformations in Metals and Alloys, (Pergamon Press, NY, 1965), 420.

large aspect ratio will reduce the stress concentration. If  $A_c$  gets very large then the right hand side becomes approximately  $=\sqrt{1/(3v_m)}$ . If we design for a stress concentration of about 2, then  $v_m$  should be greater than 8%.

### 3.4 THE ROLE OF THE ATOMIC BONDING AND STRUCTURE OF M/C INTERFACE

Throughout this section the bonding and the structure of the metal ceramic interface have been an important issue. For example, the reaction between lattice dislocation and interface dislocations will depend on the structure of the metal/ceramic interface. The climb of these interface dislocations, which is likely to control the rate of dislocation creep of the composite, will depend on interface diffusion which will be determined by atomic bonding at the interface.

Recent studies of metal ceramic interfaces by high resolution transmission electron microscopy and the modeling of the details of the defect structure of the interface is providing insights into the bonding character of the interface. For example, by this process the bonding at niobium/alumina interface is measured to be 2.5 to 3.5 times stronger than within the niobium metal.

A possible way of conceptualizing the relationship between the atomic structure of the m/c interface and physical properties is to express it as shear modulus of the interface,  $G_i$ . The relative values of  $G_i$  and the shear modulus of the metal,  $G$ , will reflect the bonding at the interface relative to the bonding within the metal. The schematic in Fig. 24 identifies some of the properties that are likely to be influenced by the relative values  $G_i$  and  $G$ . Coherent interfaces and the existence of misfit dislocations with strong lattice bending are situations where  $G_i$  is likely to be greater than  $G$ . Incoherent interfaces are likely to have weak  $G_i$ . Recent work on the niobium/alumina interface discussed at the end of the preceding paragraph, suggests that mechanical properties of a composite made from these two materials would lie in the upper left section of Fig. 24.

### 3.5 SUMMARY

The single crystal design of superalloy turbine blades represents the most advanced materials technology for reliable, high temperature structural applications. A next step in this evolution is to substitute the intermetallic phase in the superalloys by a ceramic. In this paper we have considered the influence of such a microstructure on diffusional creep, dislocation creep and thermal shock resistance. It is proposed that the volume fraction of the metal should be greater than 8%. The aspect ratio of the ceramic crystals should be greater than 30, and the transverse width of the crystals should lie in the range 1-10 $\mu$ m. For optimum thermal shock resistance the elastic moduli of the ceramic and the metal should be nearly equal. The bonding and the structure of the metal/ceramic interface is likely to control the mechanical properties of the composite, with the best properties being obtained if the elastic modulus of the interface is greater than the modulus of the metal, and if the interface is coherent.

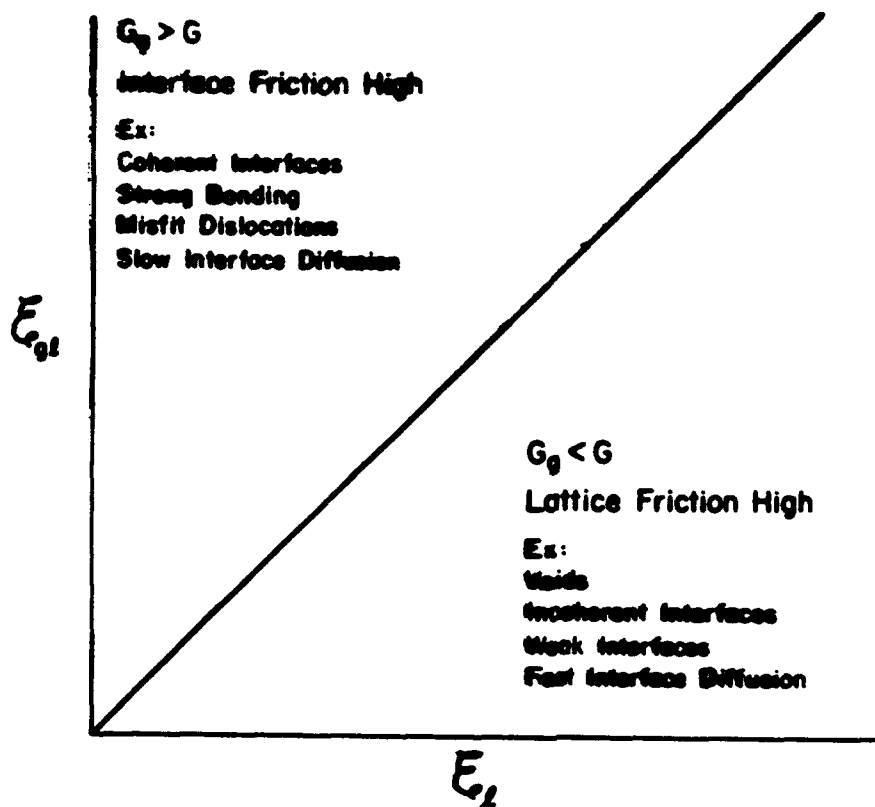


**Figure 24:** A representation of the relationship between interfacial bonding and other properties.  $G_g$  is the effective shear modulus of the interface and  $G$  is the modulus of bulk metal.

The two most important general features of the above microstructure are the sub-micrometer scale of the metal channel layers and the coherency of the metal ceramic interface. The fine scale serves to provide immunity to thermal shock. The coherent interface pins the lattice dislocations and restricts climb, and therefore, lowers the rate of dislocation creep. The details of this creep mechanism depend on understanding of the splitting of lattice dislocations into interfacial dislocations, and the climb of these dislocations together, as they remained pinned to one another.

#### 4. List of Publications and Patent.

1. "Non-Beading Thin-Film, Metal Coated Ceramic Substrate", R. Raj, U. S. Patent No: 5,173,354, issued December 22, 1992.
2. "Creep Fracture Experiments with Planar Sapphire-Copper Interfaces Stressed in Tension", C. M. Kennefick and R. Raj, Acta Metallurgica, 40, [4], 615-624 (1992).
3. "Rate Effects in Metal Ceramic Interface Sliding from the Periodic Film Cracking Technique", V. C. Jobin, R. Raj and S. L. Phoenix, Acta Metallurgica, 40, [9], 2269-2280 (1992).
4. "Scalings in Fracture Probabilities for a Brittle Matrix Fiber Composite", S. L. Phoenix and R. Raj, Acta Metallurgica, 40, [11], 2813-2828 (1992).
5. "Phase Formation and Phase Stability in the Al-Ti System", L.R. Parks, D.A. Lilienfeld, P. Borgeson and R. Raj, MRS Proceedings, 1991.
6. "In-Situ Stress Strain Response of Small Metal Particles Embedded in a Ceramic Matrix", L. R. Thompson and R. Raj, submitted to Acta Metallurgica et Materialia, September 1993.
7. "Microstructural Design of Metallic Composites for Toughness", L. R. Thompson and R. Raj, to be submitted to Acta Metallurgica et Materialia, October 1993.
8. "Single Crystal Based Microstructure Design of Metal Matrix Composites for High Temperature Applications", R. Raj, Critical Issues in the Development of High Temperature Structural Materials, Eds N. Stoloff and D. J. Duquette, Keahou Beach Hotel, Hawaii, March 1993.

## 5. Graduate Students

Ph.D. Students: L. R. Thompson  
C. M. Kennefick

M.S. Students: V. C. Jobin (partial support)